On the effect of a penetrating recirculation region on the bifurcations of the flow past a permeable sphere

M. Ciuti,[1, 2] G.A. Zampogna,[1] F. Gallaire,[1] S. Camarri,[2] and P.G. Ledda[1]

[1)] *Laboratory of Fluid Mechanics and Instabilities, École Polytechnique Fédérale de Lausanne, CH-1015 Lausanne, Switzerland*

[2)] *Dipartimento di Ingegneria Civile e Industriale, Università di Pisa, 56122 Pisa, Italy*

(*Electronic mail: pier.ledda@epfl.ch)

We study the flow past a permeable sphere modeled using homogenization theory. The flow through the porous medium is described by the Darcy law, in which the permeability quantifies the resistance for the fluid to pass through the microstructure. A slip condition on the tangential velocity at the interface between the fluid and porous region is employed to account for the viscous effects in the proximity of the interface. The steady and axisymmetric flow is first characterized under the assumption of a homogenous and isotropic porous medium. In a certain range of permeability, the recirculation region penetrates inside the sphere, resulting in a strong modification of the linear stability properties of the flow and in a decrease of the critical Reynolds numbers for the flow instability. However, for very large permeabilities, a critical permeability value is identified, beyond which the steady and axisymmetric flow remains always linearly stable. The hypothesis of a homogenous porous medium is then relaxed, and the effect of polynomial distributions of permeability inside the body is studied. Interestingly, some macroscopic flow properties do not significantly vary with the permeability distributions, provided that their average is maintained constant. The analysis is concluded by outlining a simplified procedure to retrieve the full-scale structure corresponding to a considered distribution of permeability.

I. INTRODUCTION

Aerodynamic flows past permeable bodies are the object of growing interest since they are involved in several engineering applications and natural phenomena. Aquatic vegetation plays an essential role in marine ecosystems. Ensembles of plants, the so-called canopies, deform in *honami* or *monami* shapes. They damp waves and therefore stabilize the seabed, among several other biological functions[1–3]. It is not surprising that canopy flows have received growing attention over the past decades[4,5]. Owing to the separation of scales between the size of a single plant compared to the typical extent of a canopy, the latter is often considered as a porous structure[6,7]. Canopies strongly modify turbulent flows inducing hydrodynamic instabilities, coherent structures[8–11] and fluid-structure interactions[12]. Other biological examples involve the silent flight of owls[13,14], and the transport of dandelion seeds through a parachute-like structure, called pappus, characterized by a separated recirculation region and a stable steady flow when transported by wind gusts[15–17]. Typical applications of permeable structures include filtration problems such as wastewater recovery[18,19] and fog water harvesting systems[20,21]. Porous clusters of particles are largely encountered in chemical engineering processes. Typical applications involve the dispersion in a fluid of the particles composing these clusters, because of hydrodynamic interactions[22]. Typically, these clusters are modeled as porous spherical agglomerates[23,24]. The settling of flocs and porous particles is also a common phenomenon occurring in fluidized beds and water treatment[25–28].

The presence of permeable structures strongly modifies the flow morphology, a topic of interest in the context of *passive flow control*, e.g. to quench flow instabilities. In this respect, a wide class of instabilities that received large attention in the literature concerns wake instabilities. Among the different prototypic bluff-bodies considered, the sphere is particularly important. Indeed, the wake characteristics of the impervious sphere varying the Reynolds number have been widely examined in the literature. At low Reynolds numbers, the wake presents a steady and axisymmetric toroidal recirculation eddy. A first pitchfork bifurcation with azimuthal wavenumber $|m| = 1$ occurs at $Re^* = 212.6$, consisting in a steady shift of the wake. The steady and axisymmetric wake undergoes a second instability at $Re^{**} = 280.7$[29]. Different studies have been focused on the competition between these two modes in the dynamics at large Reynolds numbers[30,31], showing the dominance of the second mode, while other authors investigated the bifurcation of the steady non-axisymmetric, bifurcated, wake (so-called *secondary* instability), finding a threshold at $Re^{***} = 271.8$[32], beyond which an alternate shedding of hairpin vortices takes place[33].

Despite this plethora of bifurcations and flow morphologies, a systematic analysis of the bifurcations that a permeable sphere encounters is still missing. Permeable structures strongly modify the flow behavior and the resulting stability properties. Castro[34] showed the flow modifications owing to the presence of holes in a flat plate. The mean recirculation region detaches from the body and the vortex shedding can be modified and eventually inhibited, as the permeability increases. Similar experimental[35] and numerical[36] investigations showed the downstream displacement of the von Kàrmàn vortex streets when cylinders composed of small fibers are employed. More recently, Steiros and Hultmark[37] developed a theoretical model to evaluate the drag for holed flat plates, which was extended by including a relation for the height and position of recirculation bubble in Steiros et al.[38]. Steiros et al.[39] investigated the effect of holes on a cylindrical circular membrane. Other studies on laminar flows through permeable bodies include the effect of porous membranes[40], airfoils[41,42], disks[43–45], rectangular[46] and square cylinders[47,48], spheres[49], and the fluid-structure interaction of porous flexible strips[50]. Porous structures are

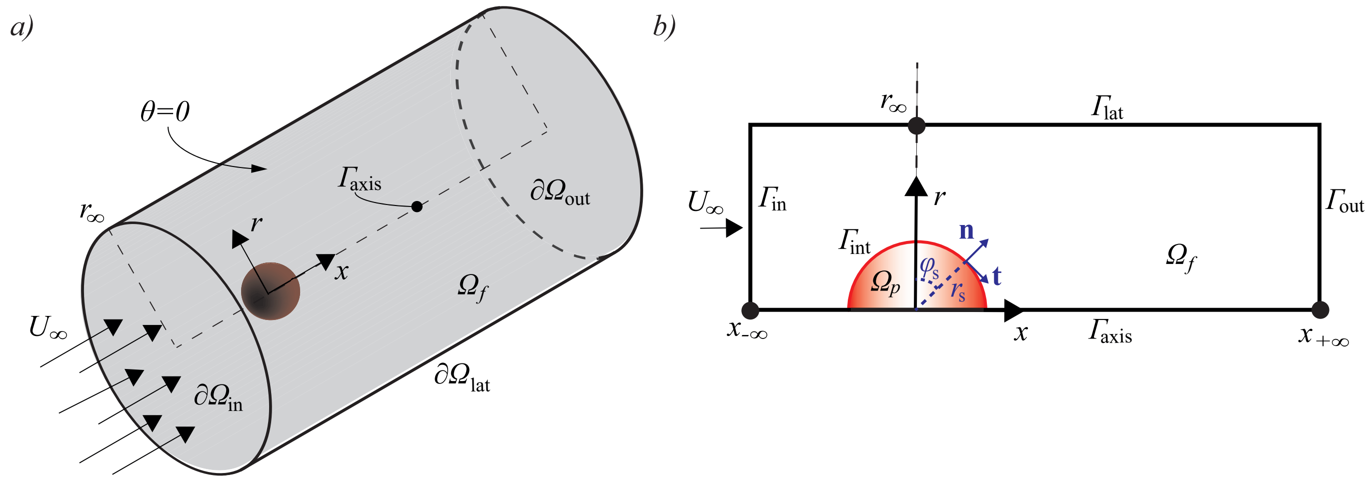

FIG. 1. *a*) Sketch of the three-dimensional flow configuration. *b*) Sketch of the computational domain employed for the axisymmetric simulations of this work, together with the global cylindrical and local spherical reference frames. The azimuthal direction is perpendicular to the represented plane.

also employed for noise reduction, both on bluff-bodies[51] and airfoils[52,53]. Owing to the large interest in the flow around permeable spheres, several works often studied the problem in the limit of negligible inertia of the fluid[23,24,54–56]. Yu et al.[49] investigated the steady and axisymmetric flow around a porous sphere. In this case, the wake can exhibit a penetrating recirculation region. Although the effect of a detached recirculation region on the stability properties of the wake has been widely investigated in the literature, the permeable sphere is identified as the perfect testing ground to study the effect of a penetrating recirculation region. In this work, the steady and axisymmetric flow past a permeable sphere and its bifurcations are studied, with constant and variable permeability properties.

The flow through the permeable sphere can be modeled via different approaches, from the well-known Darcy Law[57], where the velocity is assumed to be proportional to the pressure gradient, to its Brinkman extension[58]. In the presence of inertial effects, more complex behaviors are observed, which include symmetry breaking and unsteady instabilities within the porous medium[59]. Typical theoretical approaches are based on negligible inertia inside the porous medium and involve averaging methods[60,61], or homogenization techniques[62–65]. Homogenization techniques have the great advantage to give a direct and immediate link with the micro-structure composing the porous medium, making them suitable for optimization approaches[66]. The homogenized model, predominantly validated for simple test cases[62–65], is exploited to study an actual three-dimensional configuration of interest and highlight the potential of the direct link between micro-structure and homogenized properties through an inverse procedure to retrieve the geometry.

The use of variable permeability distributions, together with a strategy to identify a microscopic geometry that generates such permeability in practice, is a key ingredient for realistic flow control of bluff-body wakes in general and more specifically in this work for the flow past a sphere. The paper is structured as follows. Section II presents the mathematical formulation and the numerical implementation. Section III is devoted to the study of the steady and axisymmetric flow and its bifurcations for a sphere composed by a homogenous porous medium, in which the homogenized properties are taken as parameters. Section IV extends the previous results by considering variable distributions of permeability along the radius. In Section V, a procedure to retrieve the micro-structure of the sphere and verify the faithfulness of the trends observed in the parametric study is outlined.

II. MATHEMATICAL FORMULATION AND NUMERICAL IMPLEMENTATION

The mathematical formulation and the numerical implementation (whose validation is reported in Appendix A) of the problems analyzed in the present work are introduced in this section. We consider the flow of an incompressible Newtonian fluid of density ρ and viscosity μ past a permeable sphere of diameter D. The free-stream velocity is denoted as U_∞ (figure 1*a*). A cylindrical reference frame $(\bar{x}_1,\bar{x}_2,\bar{x}_3) = (\bar{x},\bar{r},\theta)$ is introduced. The velocity and pressure fields $(\bar{\mathbf{u}},\bar{p})$, indicated as $\bar{\mathbf{u}} = (\bar{u}_1,\bar{u}_2,\bar{u}_3) = (\bar{u}_x,\bar{u}_r,\bar{u}_\theta)$, satisfy the Navier Stokes equations in the fluid region Ω_f:

$$\begin{aligned} &\bar{\nabla}\cdot\bar{\mathbf{u}} = 0 \\ &\rho\left(\frac{\partial\bar{\mathbf{u}}}{\partial\bar{t}} + \bar{\mathbf{u}}\cdot\bar{\nabla}\bar{\mathbf{u}}\right) + \bar{\nabla}\bar{p} - \mu\bar{\nabla}^2\bar{\mathbf{u}} = \mathbf{0}. \end{aligned} \tag{1}$$

The flow through the porous medium Ω_p, characterized by the velocity and pressure fields $(\bar{\mathbf{v}},q)$, is described by employing the homogenized model, formally analogous to the Darcy law[62]:

$$\bar{\nabla}\bar{q} = -\mu\boldsymbol{\kappa}^{-1}\bar{\mathbf{v}}, \tag{2}$$

where $\boldsymbol{\kappa}$ is the permeability tensor. Recent homogenization-based developments rigorously defined the conditions at the interface $\partial\Omega_{int}$ between the fluid region and the porous one[64,65,67,68], which read:

$$\bar{\mathbf{u}} - \left(-\frac{\boldsymbol{\kappa}_{\text{int}}}{\mu}\bar{\nabla}\bar{q}\right) = \bar{\boldsymbol{\Lambda}}\left[\bar{\Sigma}(\bar{\mathbf{u}},\bar{p})\mathbf{n}\right], \quad \bar{q} = -\left[\bar{\Sigma}(\bar{\mathbf{u}},\bar{p})\mathbf{n}\right]\cdot\mathbf{n} \quad (3)$$

where $\bar{\Sigma}(\bar{\mathbf{u}},\bar{p}) = -\bar{p}\mathbf{I} + \mu\left(\bar{\nabla}\bar{\mathbf{u}} + \bar{\nabla}\bar{\mathbf{u}}^T\right)$ and $\boldsymbol{\kappa}_{\text{int}}$ represents the permeability tensor evaluated at the interface (which does not necessarily coincide with the bulk one $\boldsymbol{\kappa}$) and $\bar{\boldsymbol{\Lambda}}$ is the slip tensor. The spherical coordinates radius, colatitude and azimuth $(r_s, \varphi_s, \theta_s = \theta)$ are introduced, whose origin is located at the center of the sphere (see figure 1). At the sphere surface, $\mathbf{t}$, $\mathbf{s}$ and $\mathbf{n}$ are the corresponding colatitude, azimuth and radial unit vectors. In this spherical reference frame, the slip tensor reads:

$$\bar{\boldsymbol{\Lambda}} = \begin{pmatrix} \bar{\Lambda}_t & 0 & 0 \\ 0 & \bar{\Lambda}_s & 0 \\ 0 & 0 & 0 \end{pmatrix} \quad (4)$$

The slip tensor is thus projected onto the cylindrical reference frame employed in this work by introducing the notation $(\mathbf{a}\otimes\mathbf{b})_{ij} = a_i b_j$, obtaining as a result[69]:

$$\bar{\boldsymbol{\Lambda}} = \bar{\Lambda}_t \mathbf{t}\otimes\mathbf{t} + \bar{\Lambda}_s \mathbf{s}\otimes\mathbf{s}, \quad (5)$$

where $\mathbf{t}$ and $\mathbf{s}$ are expressed in the cylindrical reference frame. The macroscopic quantities, denoted here as permeability, interfacial permeability and slip, actually represent the macroscopic effects of a given microscopic structure on the flow field. In Appendix B the formal problems which link the microscopic structure to these quantities are given, while in sections III and IV they are treated as free parameters to characterize the flow past a porous sphere. Depending on the values of the homogenized tensors, some limiting cases are identified. The case $\boldsymbol{\kappa} = \boldsymbol{\kappa}_{\text{itf}} = \mathbf{0}$ with $\bar{\boldsymbol{\Lambda}} \neq \mathbf{0}$ is equivalent to a first-order slip condition on a textured surface of a solid sphere[69], since no flow occurs inside the body and the velocity normal to the surface is neglected. Another limiting condition occurs when $\boldsymbol{\kappa} \to \infty$ and $\boldsymbol{\kappa}_{\text{itf}} \to \infty$. In this case, the porous structure does not induce any resistance to the flow, which is equivalent to the absence of a solid structure. Finally, the condition $\bar{\boldsymbol{\Lambda}} = \mathbf{0}$ means that the viscous diffusion effects in the proximity of the fluid-porous interface are neglected.

The macroscopic flow problem is completed by the far-field boundary conditions in the fluid domain. At the inlet, a uniform free stream is imposed, i.e. $\bar{\mathbf{u}} = U_\infty \mathbf{e}_x$, while on the lateral and outlet boundaries a zero-stress condition is imposed, $\bar{\Sigma}(\bar{\mathbf{u}},\bar{p})\mathbf{n} = \mathbf{0}$. The flow equations are non-dimensionalized by introducing the characteristic length D (the sphere diameter), velocity U_∞, time $\frac{D}{U_\infty}$ and pressure ρU_∞^2, obtaining the following set of non-dimensional equations:

$$\begin{cases} \nabla\cdot\mathbf{u} = 0 \\ \frac{\partial\mathbf{u}}{\partial t} + \mathbf{u}\cdot\nabla\mathbf{u} + \nabla p - \frac{1}{Re}\nabla^2\mathbf{u} = \mathbf{0} \end{cases} \quad \Omega_f, \quad (6)$$

$$\begin{cases} \mathbf{v} = -Re\mathbf{Da}\nabla q \\ \nabla\cdot\mathbf{v} = 0 \end{cases} \quad \Omega_p, \quad (7)$$

together with the non-dimensional interface conditions at $\partial\Omega_{\text{int}}$:

$$\mathbf{u} - (-Re\mathbf{Da}_{\text{int}}\nabla q) = \boldsymbol{\Lambda}\left[\Sigma(\mathbf{u},p)\mathbf{n}\right], \quad q = -\left[\Sigma(\mathbf{u},p)\mathbf{n}\right]\cdot\mathbf{n}, \quad (8)$$

where $\Sigma(\mathbf{u},p) = -p\mathbf{I} + \frac{1}{Re}\left(\nabla\mathbf{u} + \nabla\mathbf{u}^T\right)$ is the non-dimensional stress tensor, $Re = \frac{U_\infty D}{\nu}$ is the Reynolds number, $\mathbf{Da} = \frac{\boldsymbol{\kappa}}{D^2}$ and $\mathbf{Da}_{\text{int}} = \frac{\boldsymbol{\kappa}_{\text{int}}}{D^2}$ are respectively the Darcy tensor in the bulk and at the interface, and $\boldsymbol{\Lambda} = \frac{\bar{\boldsymbol{\Lambda}}}{D}$ is the slip tensor, whose non-zero diagonal components are denoted with Λ_t and Λ_s, respectively along the colatitude and azimuthal directions.

In this work, we focus on the steady and axisymmetric solution (i.e. $\partial/\partial t = 0$ and $\partial/\partial\theta = 0$) of the flow equations (6,7), so-called baseflow, and its stability with respect to azimuthal disturbances, i.e. the perturbation is expanded in normal modes along the azimuthal direction. Therefore, to compute the baseflow, the flow equations are solved in the azimuthal plane $\theta = 0$, leading to the two-dimensional domain reported in figure 1*b*. The steady and axisymmetric solution of the equations $(\mathbf{U},P,\mathbf{V},Q)$, with $\mathbf{U} = (U_x,U_r)$ and $\mathbf{V} = (V_x,V_r)$, satisfies the following set of equations:

$$\begin{cases} \nabla\cdot\mathbf{U} = 0 \\ \mathbf{U}\cdot\nabla\mathbf{U} + \nabla P - \frac{1}{Re}\nabla^2\mathbf{U} = \mathbf{0} \end{cases} \quad \Omega_f, \quad (9)$$

$$\begin{cases} \mathbf{V} = -Re\mathbf{Da}\nabla Q \\ \nabla\cdot\mathbf{V} = 0 \end{cases} \quad \Omega_p, \quad (10)$$

together with the non-dimensional interface conditions at Γ_{int}:

$$\mathbf{U} - (-Re\mathbf{Da}_{\text{int}}\nabla Q) = \boldsymbol{\Lambda}\left[\Sigma(\mathbf{U},P)\mathbf{n}\right], \quad Q = -\left[\Sigma(\mathbf{U},P)\mathbf{n}\right]\cdot\mathbf{n}. \quad (11)$$

The remaining boundary conditions to be imposed are the free-stream condition $\mathbf{U} = \mathbf{e}_x = [1,0,0]^T$ at Γ_{inlet}, the free-stress condition $\Sigma(\mathbf{U},P)\mathbf{n} = \mathbf{0}$ at $\Gamma_{\text{lat}}\cup\Gamma_{\text{out}}$, and the boundary condition for the fluid region $\mathbf{U}\cdot\mathbf{e}_r = U_r = 0$ on the axis Γ_{axis}.

As mentioned above, the stability properties to perturbations of the baseflow $(\mathbf{U},P)$ are investigated. To this purpose, a normal mode decomposition of azimuthal wavenumber m and complex frequency σ is considered, whose real and imaginary parts are respectively the growth rate and the frequency. The following ansatz has been introduced

$$\begin{bmatrix} \mathbf{u} \\ p \\ \mathbf{v} \\ q \end{bmatrix} = \begin{bmatrix} \mathbf{U}(x,r) \\ P(x,r) \\ \mathbf{V}(x,r) \\ Q(x,r) \end{bmatrix} + \varsigma \begin{bmatrix} \hat{\mathbf{u}}(x,r) \\ \hat{p}(x,r) \\ \hat{\mathbf{v}}(x,r) \\ \hat{q}(x,r) \end{bmatrix} \exp\left(\mathrm{i}m\theta + \sigma t\right), \quad (12)$$

$\varsigma \ll 1$. The flow equations (6,7), with the corresponding boundary conditions, are expanded in powers of ς, using the expression for the flow field given in equation (12). At order $\mathscr{O}(1)$, the baseflow equations for $(\mathbf{U},P,\ \mathbf{V},Q)$ are retrieved, while at order $\mathscr{O}(\varsigma)$ one obtains:

$$\begin{cases} \nabla\cdot\hat{\mathbf{u}} = 0 \\ \sigma\hat{\mathbf{u}} + \mathbf{U}\cdot\nabla_m\hat{\mathbf{u}} + \hat{\mathbf{u}}\cdot\nabla_0\mathbf{U} + \nabla_m\hat{p} - \frac{1}{Re}\nabla_m^2\hat{\mathbf{u}} = \mathbf{0} \end{cases} \quad \Omega_f, \quad (13)$$

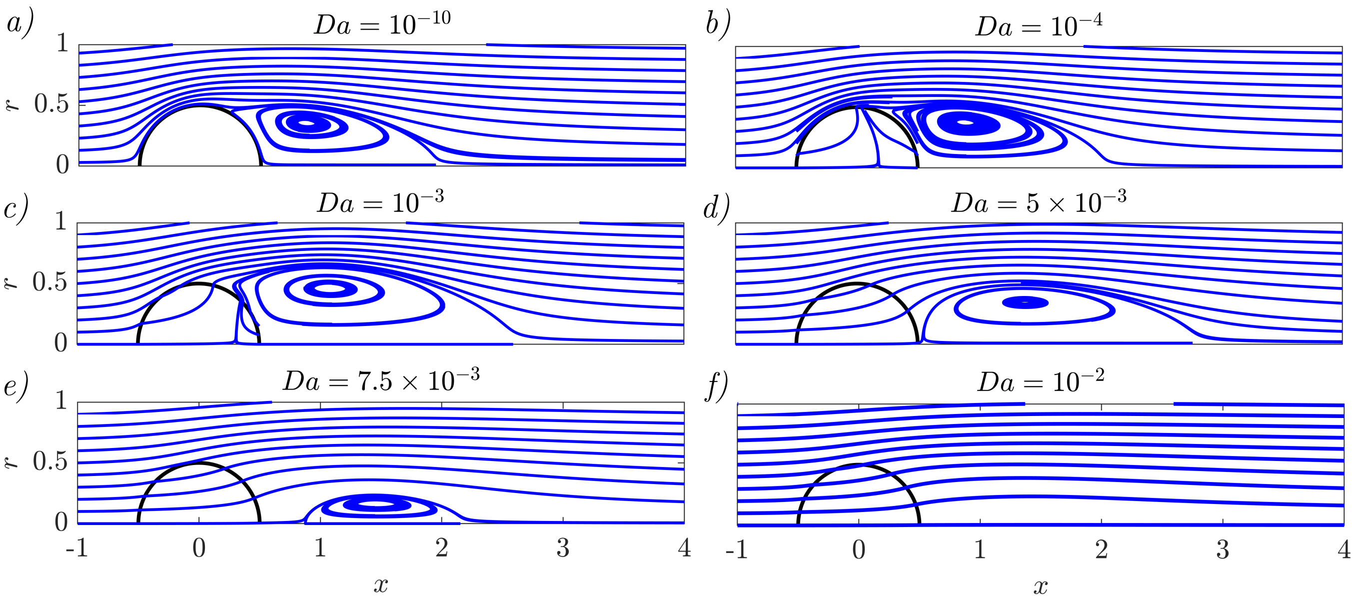

FIG. 2. Streamlines of the axisymmetric flow past a permeable sphere for $Re = 200$, $\Lambda_t = 0$ and different values of Da: *a)* $Da = 10^{-10}$, *b)* $Da = 10^{-4}$, *c)* $Da = 10^{-3}$, *d)* $Da = 5 \times 10^{-3}$, *e)* $Da = 7.5 \times 10^{-3}$, *f)* $Da = 10^{-2}$.

$$\begin{cases} \hat{\mathbf{v}} = -Re\mathbf{Da}\nabla_m \hat{q} \\ \nabla_m \cdot \hat{\mathbf{v}} = 0 \end{cases} \quad \Omega_p, \tag{14}$$

$$\hat{\mathbf{u}} - (-Re\mathbf{Da}_{\text{int}} \nabla_m \hat{q}) = \mathbf{\Lambda} \left[\Sigma(\hat{\mathbf{u}}, \hat{p}) \mathbf{n} \right], \quad \hat{q} = -\left[\Sigma_m(\hat{\mathbf{u}}, \hat{p}) \mathbf{n} \right] \cdot \mathbf{n}, \tag{15}$$

where the following operators are introduced[29]

$$\nabla_m f = \begin{bmatrix} \frac{\partial f}{\partial x} \\ \frac{\partial f}{\partial r} \\ \frac{imf}{r} \end{bmatrix}, \tag{16}$$

$$\nabla_m \mathbf{g} = \begin{bmatrix} \frac{\partial g_x}{\partial x} & \frac{\partial g_x}{\partial r} & \frac{im}{r} g_x \\ \frac{\partial g_r}{\partial x} & \frac{\partial g_r}{\partial r} & \frac{im}{r} g_r - \frac{g_\theta}{r} \\ \frac{\partial g_\theta}{\partial x} & \frac{\partial g_\theta}{\partial r} & \frac{im}{r} g_\theta + \frac{g_r}{r} \end{bmatrix}, \tag{17}$$

$$\nabla_m \cdot \mathbf{g} = \frac{\partial g_x}{\partial x} + \frac{1}{r} \frac{\partial r g_r}{\partial r} + \frac{im}{r} g_\theta, \tag{18}$$

$$\nabla_m^2 \mathbf{g} = \nabla_m \cdot (\nabla_m \mathbf{g}), \tag{19}$$

$$\Sigma_m(\mathbf{g}, f) = -g\mathbf{I} + \frac{1}{Re} \left(\nabla_m \mathbf{g} + \nabla_m \mathbf{g}^T \right). \tag{20}$$

The homogenous condition $\hat{\mathbf{u}} = \mathbf{0}$ is imposed at the inlet, while on the lateral and outlet boundary the free-stress condition $\Sigma_m(\mathbf{u}, p)\mathbf{n} = \mathbf{0}$ is enforced. On the axis, the following regularity conditions have to be imposed[29,70,71]:

$$u_r = u_\theta = \frac{\partial u_x}{\partial r} = 0 \quad \text{for} \ \ m = 0; \tag{21}$$

$$\frac{\partial u_r}{\partial r} = u_x = \frac{\partial u_\theta}{\partial r} = 0 \quad \text{for} \ \ |m| = 1; \tag{22}$$

$$u_r = u_\theta = u_x = 0 \quad \text{for} \ \ |m| > 1; \tag{23}$$

The outlined set of equations is an eigenvalue problem of complex eigenvalues $\sigma = \text{Re}(\sigma) + \text{iIm}(\sigma)$, whose real part is the growth rate of the global mode, and the imaginary part is its angular velocity. The flow is asymptotically unstable if at least one eigenvalue has a positive real part; otherwise, the flow is asymptotically stable. Therefore, stable modes are characterized by $\text{Re}(\sigma) < 0$, while unstable ones by $\text{Re}(\sigma) > 0$.

A. Numerical implementation of the flow equations

The numerical implementation of the flow equations is performed in COMSOL Multiphysics. The steady equations (9,10) and the eigenvalues problem (13,14) are implemented through their weak form, employing $P2-P1$ Taylor-Hood elements for the fluid domain. The steady solutions are obtained via the built-in Netwon algorithm, with a relative tolerance of 10^{-6}, while the eigenvalue problem is solved by employing the built-in eigenvalue solver based on the ARPACK library. The numerical implementation of the Darcy law is based on a second-order PDE for q obtained by taking the divergence of equation (7):

$$\nabla \cdot \mathbf{v} = -Re\nabla \cdot (\mathbf{Da}\nabla q) = 0 \Rightarrow \nabla \cdot (\mathbf{Da}\nabla q) = 0. \tag{24}$$

The latter formulation holds both for the baseflow and linear stability analysis formulation, substituting q with Q and $\hat{q}$, respectively, for which $P1$ elements are employed. The two problems are numerically coupled via an implementation of the domain decomposition method[72], where the free-fluid and the porous region exchange information thanks to equations (15). The interface conditions on the free-fluid velocity and

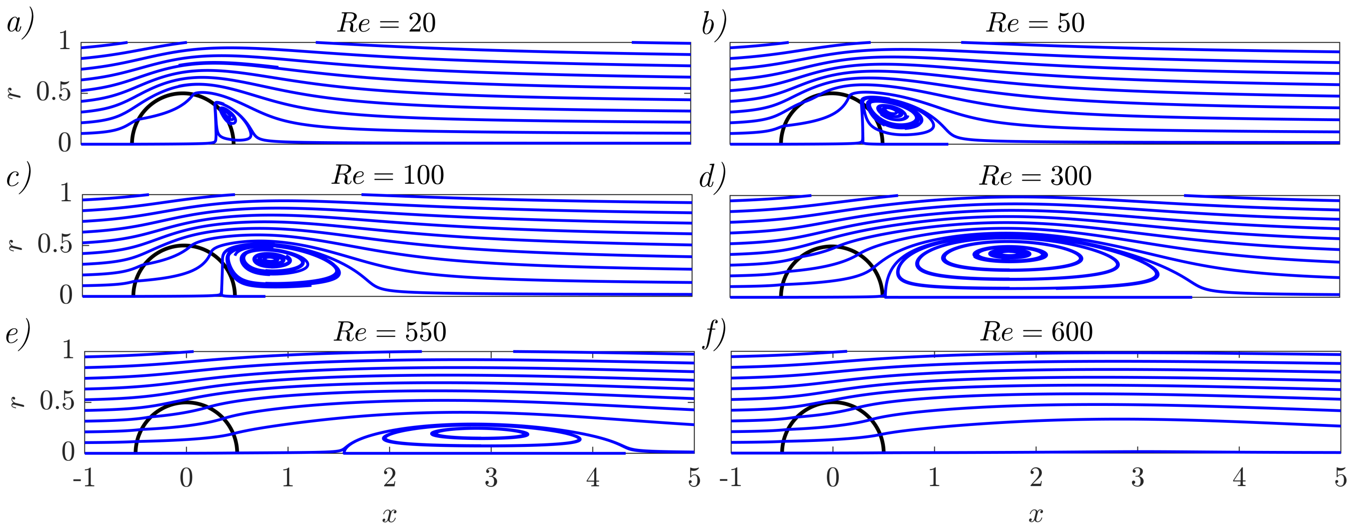

FIG. 3. Streamlines of the axisymmetric flow past a permeable sphere, for $Da = 3.5\times10^{-3}$, $\Lambda_t = 0$ and different values of Re: *a*) $Re = 20$, *b*) $Re = 50$, *c*) $Re = 100$, *d*) $Re = 300$, *e*) $Re = 550$, *f*) $Re = 600$.

Darcy pressure are imposed via a Dirichlet boundary condition on Γ_{int}. The results of the convergence analysis in terms of domain size and discretization are reported in Appendix A.

III. WAKE FLOWS PAST SPHERES OF CONSTANT PERMEABILITY

The flow past a sphere of constant permeability is investigated in the present section. A locally isotropic Darcy tensor is considered, i.e. in cylindrical coordinates $\mathbf{Da} = Da\mathbf{I}$, where Da is the Darcy number. Typically, in a homogenous porous medium, the interfacial Darcy number is slightly larger to the bulk one $\mathbf{Da}_{\text{int}} \geq \mathbf{Da}$ owing to the different boundary conditions applying in the proximity of the interface, but of the same order of magnitude[64]. Since in this section both $\mathbf{Da}$ and $\mathbf{Da}_{\text{int}}$ are treated as free-parameters, for the sake of simplicity the interface permeability is assumed to be equal to the bulk one, i.e. $\mathbf{Da}_{\text{int}} = \mathbf{Da}$. As concerns the slip tensor $\mathbf{\Lambda}$, the steady and axisymmetric wake is influenced only by Λ_t, since Λ_s appears when the azimuthal direction is considered. However, the latter affects the linear stability analysis results. In the first stage, we impose $\Lambda_t = \Lambda_s = 0$ and the effect of the sole Darcy number is investigated. In the second stage, the effects of positive entries in the slip tensor are studied.

A. Steady and axisymmetric flow

The steady and axisymmetric flow past a permeable sphere is now described. Previous works showed that the wake past permeable bodies is characterized by a recirculation region that moves downstream and becomes smaller as the permeability increases[46]. However, as already noted by Yu et al.[49] with a different porous model and for $Re < 200$, the flow past a permeable sphere may present a recirculation region that penetrates inside the body. Figure 2 shows the flow streamlines for a fixed Reynolds number $Re = 200$ and for different values of Da. At very low values of Da, the flow is analogous to the solid case. However, already at $Da = 10^{-4}$, the recirculation region penetrates in the rear of the sphere, with non-negligible values of the velocity. A closer look at the frontal part of the sphere shows that the streamlines entering inside the body tend to diverge and the flow leaves the body in the vicinity of the upper region of the sphere, upstream of the point beyond which the streamline that identifies the recirculation region starts. Increasing the permeability, the recirculation region increases its dimensions, as shown for $Da = 10^{-3}$ and $Da = 5\times10^{-3}$. At $Da = 7.5\times10^{-3}$, the recirculation becomes extremely small and detached from the body, while at $Da = 10^{-2}$ it eventually disappears.

Figure 3 shows the effect of the Reynolds number, for fixed $Da = 3.5\times10^{-3}$. At $Re \approx 20$, a penetrating recirculation region develops, whose core is located close to the fluid-porous interface. As the Reynolds number increases, the recirculation region moves downstream, while increasing its dimensions. At $Re = 300$, the recirculation region leaves the body; a further increase in Re leads to smaller recirculations, and eventually their suppression at very large Re.

From a quantitative viewpoint, the recirculation region boundary is defined by the streamline which presents two zeros of the streamwise component of the velocity $u_x = 0$ along $r = 0$. The length of the recirculation region L_r is thus the distance between these two points, measured along the z axis. The distance between the rear of the sphere and the recirculation region X_r is instead the streamwise location, from the point $x = 0.5$, of the first zero of the axial velocity. X_r is negative whenever the recirculation region starts inside the body. The results are reported in figure 4. For fixed Re, an increase in the Darcy number leads to an increase in the length of the recirculation region. However, at very large permeabilities, a steep decrease of the size of the recirculation is observed, un-

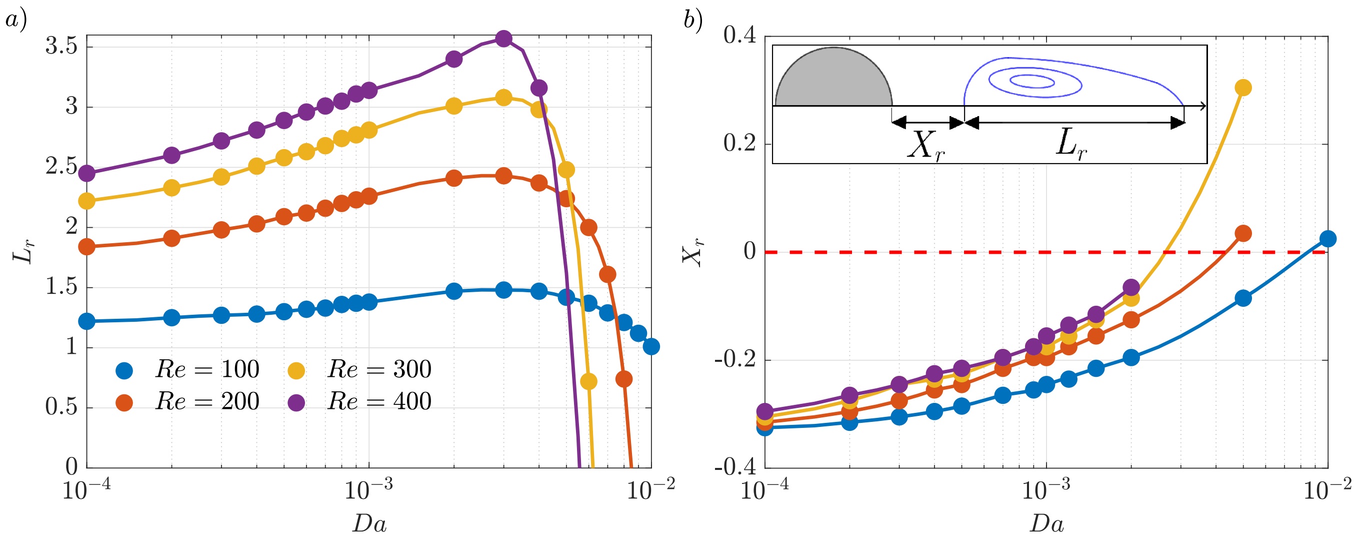

FIG. 4. Variation of a) the length of the recirculation region L_r and b) its distance from the rear of the sphere, X_r, with Da, in case of $\Lambda_t = 0$ and for different values of Re.

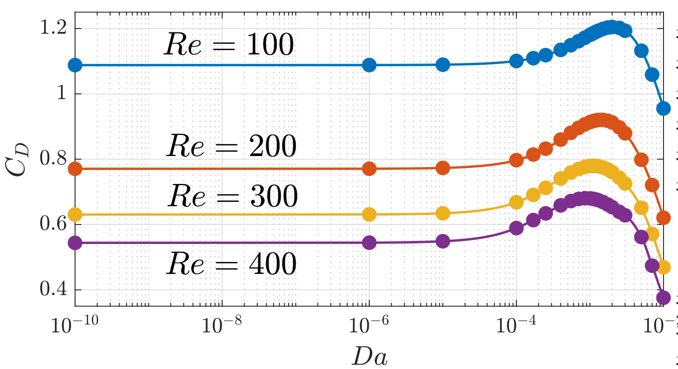

FIG. 5. Variation of the drag coefficient with Da, in case of $\Lambda_t = 0$ and for different values of Re.

til the recirculation disappears. This effect is observed in the whole range of Re and is enhanced as the latter increases. We finally note that the distance of the recirculation region from the rear is negative (i.e. the recirculation penetrates inside the sphere) in a large range of the considered parameters, and becomes positive only at very large permeabilities and Reynolds numbers.

The initial increase of L_r can be correlated to the streamlines in figure 2. While in the solid case there is no flow, in the permeable case the flow passes through the body. Because of the presence of a massive separation, the strong recirculation has enough momentum to overcome the resistance to penetrate inside the rear of the sphere. As Da increases, the velocities inside the body increase while the separation point on the interface does not move appreciably. The presence of larger velocities at the interface enhances the gradients and thus the vorticity, whose effect is an increase of the counterflow generating the recirculation bubble. However, this mechanism enters in competition with the velocity gradients reduction as the body becomes more permeable. As a net effect, the separation point moves downstream until it leaves the body, as the recirculation becomes progressively smaller until it disappears.

The analysis of the steady and axisymmetric wake continues by considering the drag coefficient, defined in non-dimensional form as:

$$C_D = 16 \int_{\Gamma_{\text{int}}} [\Sigma(\mathbf{U}, P) \cdot \mathbf{n}] \cdot \mathbf{e}_x \mathrm{d}\Gamma. \tag{25}$$

Figure 5 shows the variation of C_D with Da, for different values of Re. The drag coefficient increases with Da, reaches a maximum and decreases. However, this decrease is observed at extremely large permeabilities. This non-monotonous behavior relates to the one of the recirculation region, since both the drag coefficient and the recirculation size are a trace of the vorticity production[46].

The analysis of the steady and axisymmetric wake past a permeable sphere showed results similar to those obtained in Yu et al.[49], although they are obtained here with a different formulation for the flow through the porous medium. In opposition to permeable rectangles[46], thin disks[16,43] (characterized by detached recirculation regions) and circular[73] and square cylinders[46] (characterized by a weak penetration of the recirculation inside the body), the permeable sphere is characterized by the presence of penetration of the recirculation region in a large range of the parameters space. Similar penetrating recirculation regions were observed in a limited parameter range by Tang et al.[45], for thick disks. The presence of penetration of the recirculation region inside the body is related to (i) the finite extent of the body compared to two-dimensional shapes and (ii) the streamline configuration assumed by the particular axisymmetric shape considered here, i.e. the sphere. The finite size of the body compared to nominally two-dimensional plane shapes imposes a smaller perturbation of the flow, and thus the fluid experiences less resistance to pass through the body. The spherical shape also enhances this behavior because of its streamwise extent, which

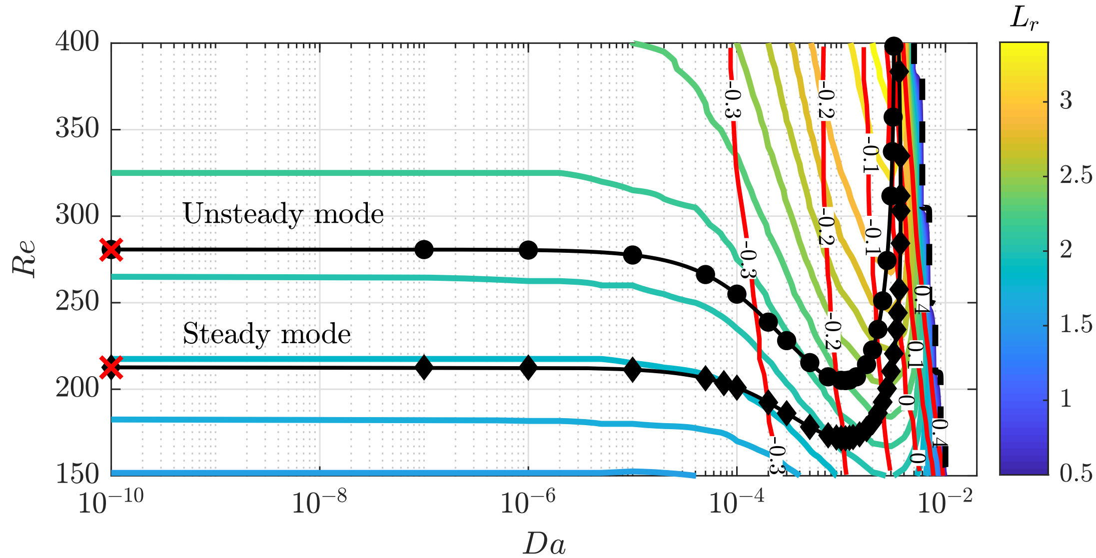

FIG. 6. Bifurcation diagram in the $Da-Re$ plane, for $\Lambda_t = 0$. The black curve with diamonds denotes the critical Reynolds number for the first bifurcation, beyond which the steady eigenvalue is unstable, while the black one with dots denotes the critical Reynolds number for the second and unsteady bifurcation. The red crosses denote the values of the critical Reynolds numbers for the solid case. The colored and red iso-contours denote the values of the length of the recirculation region L_r and its distance from the rear X_r, respectively. The iso-level $L_r = 0$ is highlighted in black dashed line.

allows the recirculation region to penetrate and the separation point at the interface to not move significantly while the inner velocities are increasing with Da. However, at some point, the sphere becomes extremely permeable and finally behaves as the other porous bluff-bodies already considered in the literature.

In this section, we described the steady and axisymmetric solution of the flow past a permeable sphere. However, not all the described configurations are likely to be observed. In the next section, we identify, via linear stability analysis, the regions of the parameters space where the steady and axisymmetric solution is linearly stable. Where instead such solutions are unstable, the possible non-steady and non-axisymmetric flow structures are characterized.

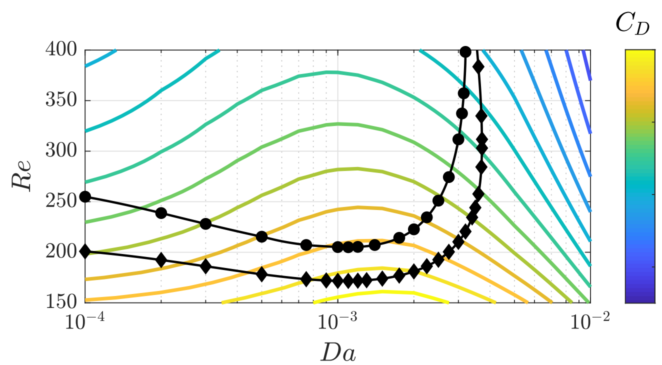

FIG. 7. Iso-contours of the drag coefficient C_D in the $Da-Re$ plane superimposed onto the bifurcation diagram, for $\Lambda_t = 0$. The black curve with diamonds denotes the critical Reynolds number for the first bifurcation, beyond which the steady eigenvalue is unstable, while the black one with dots denotes the critical Reynolds number for the second and unsteady bifurcation.

B. Stability analysis of the steady and axisymmetric flow

As introduced in Section II, a perturbation in normal form, of azimuthal wavenumber m, is considered. The wake past a solid sphere presents two bifurcations[29], which occur for $|m| = 1$. The first one occurs at $Re = 212.6$ and it is characterized by $\mathrm{Im}(\sigma) = 0$, i.e. the mode does not oscillate in time. In the non-linear regime, the mode saturates, leading to a steady breaking of the axisymmetry. We thus refer to this mode as the *steady* mode, always considering that, in the linear regime, it presents a pure exponential growth in time. The second bifurcation of the steady and axisymmetric wake occurs at $Re = 280.7$ and is an alternate shedding of vortices, which will be called *unsteady* mode.

Since here we focus on the effect of the permeability on the steady and axisymmetric wake and the eventual suppression of these instabilities, the behavior of these two unstable modes, with azimuthal wavenumber $m = 1$, is studied. The regions in the parameters space in which these two modes present a null growth rate, i.e. the so-called marginal or neutral stability conditions, are first identified.

Figure 6 reports the marginal stability curves for the two modes in the $Da-Re$ plane. We initially consider a fixed $Da = 10^{-10}$ with an increase of the Reynolds number. For $Re < 212.6$, all eigenvalues have a negative real part and thus the steady and axisymmetric wake is stable. At $Re = 212.6$, the steady mode is in the neutral stability condition, and beyond it becomes unstable. At $Re = 280.7$, the unsteady mode becomes unstable. In the range $10^{-10} < Da < 10^{-6}$, the crit-

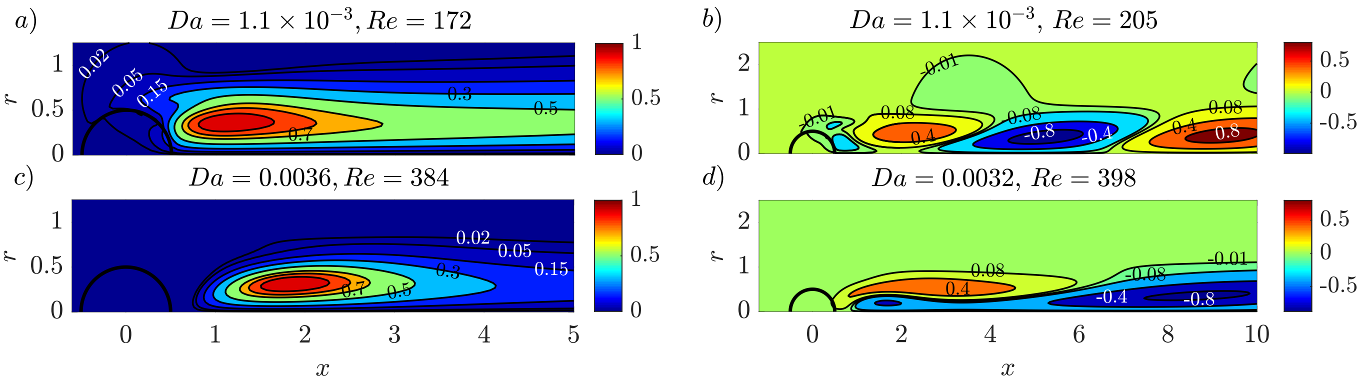

FIG. 8. Iso-contours of the real part of the streamwise component of the velocity field, rescaled with its maximum absolute value, for the (a,c) steady and (b,d) unsteady modes, at the marginal stability, for $\Lambda_t = 0$.

ical Reynolds numbers are constant. For larger Da, the critical Reynolds number decreases more and more quickly until both curves reach a minimum. The marginal stability curves of both the steady and unsteady modes exhibit the minima at $Re = 171.7$ and $Re = 205.1$, respectively, at the same value of $Da = 1.1 \times 10^{-3}$. Below $Re = 171.7$, the steady and axisymmetric wake is thus linearly stable independently of Da. For larger Da, the critical Reynolds numbers drastically increase, with a slight inversion of the curves, i.e. for fixed Da the mode becomes unstable and then stable again as Re increases, similarly to the behavior observed in Ledda et al.[16,46] for different bluff bodies. A critical value of the Darcy number $Da = 3.7 \times 10^{-3}$ is finally obtained, beyond which the steady and axisymmetric wake is linearly stable independently of Re.

Three regions in the parameters space (Re, Da) are identified: one in which the steady and axisymmetric wake is stable, one in which the steady mode is unstable, and one in which both the steady and unsteady modes are unstable. In contrast to other bluff body wakes [16,46], the critical Reynolds numbers for the porous sphere drastically decrease as the permeability increases, and the complete stabilization of the flow independently of Re is reached only for very large values of Da, while at intermediate values of Da the flow instability is anticipated by the permeability. This behavior occurs when the recirculation region is penetrating inside the sphere. Therefore, the wake of a permeable sphere is more unstable to perturbations compared to the solid one. This counterintuitive behavior vanishes at very large permeabilities, in which the recirculation region moves downstream of the body and eventually disappears. According to Monkewitz[74] and the recent analyses of Ledda et al.[46], the wake instability is correlated to the extent of the recirculation region, which roughly identifies the instability core[75]. Therefore, the iso-levels of the length of the recirculation region follow a trend similar to the marginal stability curves. The iso-levels of L_r indeed follow the same trend, as shown in figure 6. In particular, L_r initially increases with Da, while Re_{cr} decreases, and successively L_r decreases rapidly and Re_{cr} increases. The deviations in the proximity of the minimum of Re_{cr} may be related to the change of the velocity profiles composing the wake at each streamwise location[74]. The iso-levels of X_r become positive

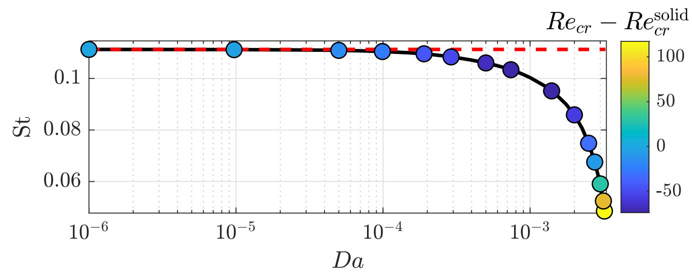

FIG. 9. Variation of the Strouhal number $\mathrm{St} = \mathrm{Im}(\sigma)/(2\pi)$ of the unsteady mode with Da, following the marginal stability curve for the unsteady instability. The colored dots denote the values of $Re_{cr} - Re_{cr}^{\mathrm{solid}}$, where $Re_{cr}^{\mathrm{solid}} = 280.7$.

close to the critical Darcy number for unconditional stability. Therefore, the marginal stability curves trend is related to the presence of a penetrating recirculation region.

Figure 7 shows the iso-contours of the drag coefficient in the $Da - Re$ plane together with the marginal stability curves. For fixed Re, the maximum of drag is attained at $Da \approx 10^{-3}$, in the vicinity of the minima in the Reynolds numbers of the marginal stability curves. This observation can be explained considering the correlation between the extent of the recirculation region and the critical Reynolds number. The drag increase is predominantly related to the decrease of the pressure in the rear part of the body, similarly to the case of a circular membrane[66]. Stronger counterflow velocities imply, with a good approximation, smaller pressure values in the rear part and thus a positive drag contribution. At the same time, larger counterflows imply larger recirculation regions[46]. Larger values of C_D are thus related to larger values of L_r, and a more unstable wake, as previously discussed[46,74], i.e. the maximum drag is attained in the vicinity of the marginal stability curves minima.

While previous works described the downstream displacement of the mode[46], it is not clear if the latter can move upstream and penetrate inside the body due to the penetrating recirculation region. Figures 8a,b) show the unstable modes at the marginal stability conditions corresponding to the minima of the marginal stability curves (see details pro-

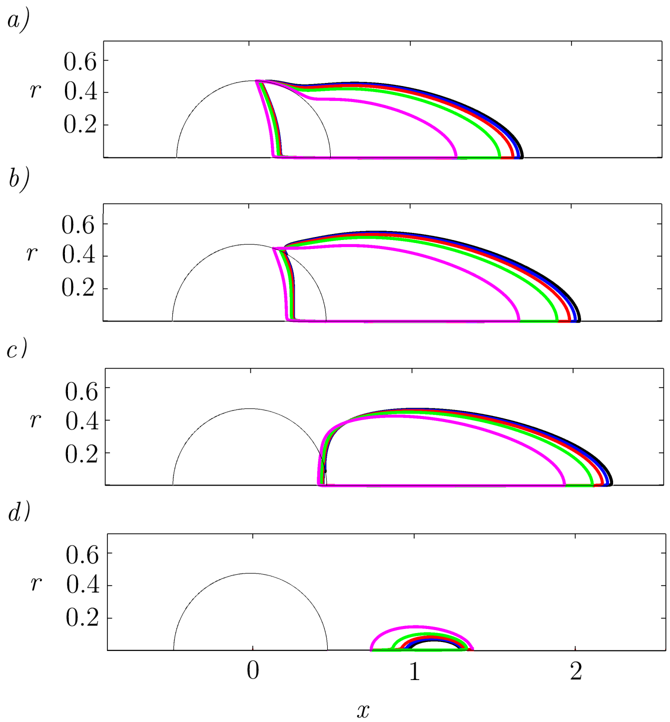

FIG. 10. Streamline identifying the recirculation region for $Re = 150$, $a)$ $Da = 10^{-4}$, $b)$ $Da = 10^{-3}$, $c)$ $Da = 5\times10^{-3}$, $d)$ $Da = 10^{-2}$. The different colors correspond to $\Lambda_t = 10^{-4}$ (black), $\Lambda_t = 10^{-3}$ (blue), $\Lambda_t = 5\times10^{-3}$ (red), $\Lambda_t = 10^{-2}$ (green), $\Lambda_t = 5\times10^{-2}$ (magenta).

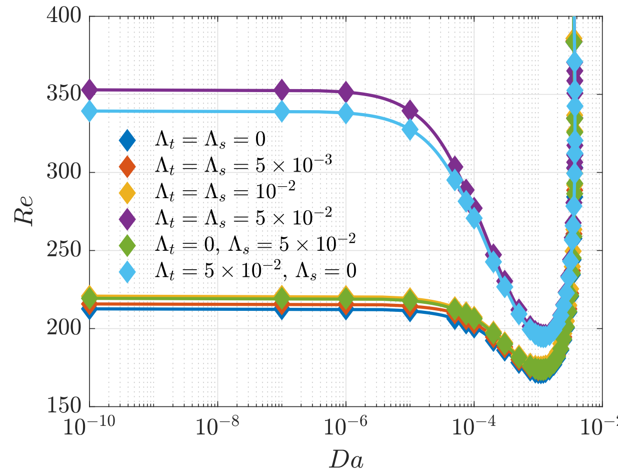

FIG. 11. Marginal stability curves, for the first bifurcation, for different values of Λ_t and Λ_s.

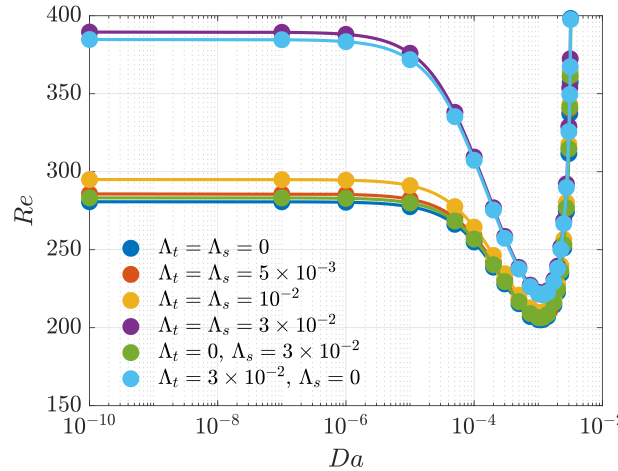

FIG. 12. Marginal stability curves, for the second bifurcation, for different values of Λ_t and Λ_s.

vided in the figure legend). The instability also develops inside the sphere, even if the associated magnitude is 10^{-2} times lower than the values attained outside, in particular for the unsteady mode. Therefore, an upstream displacement of the mode together with the recirculation region, which penetrates inside the porous sphere, is observed. An increase of the Reynolds number following the marginal stability curve leads to a downstream displacement of the steady mode (figure 8c), while the unsteady mode (figure 8d) is characterized by a periodic distribution with larger streamwise wavelength compared to case b). The resulting unsteady mode is thus characterized by a periodic shedding of vortical structures, whose streamwise wavelength increases with Re, following the marginal stability curve. As a consequence, the shedding frequency of these vortical structures decreases with Da, a conclusion which is quantitatively supported by figure 9. The imaginary part of the eigenvalue, which represents the shedding frequency, strongly decreases for $Da > 10^{-3}$.

In this section, we highlighted the peculiarities of the penetrating recirculation region and its consequences on the flow stability. In the following, we consider positive values of the slip tensor components.

C. Effect of the slip length

The previous sections focused on the permeability effect on the flow past a sphere in the absence of slip. These results are complemented by including the effect of a difference in the velocity at the fluid-porous interface. In the stability analysis, also the azimuthal component of the slip tensor Λ_s has to be considered, owing to the presence of the azimuthal velocity perturbation.

Figure 10 shows the streamlines identifying the recirculation region for $Re = 150$. In each frame, Da is fixed and Λ_t varies in the range $10^{-4} < \Lambda_t < 5\times10^{-2}$. The introduction of a finite slip length in the problem does not significantly affect the flow morphology, although some differences can be observed. An increase in Λ_t slightly modifies the position of the flow separation points and the recirculation region. At low permeabilities, larger values of slip imply smaller recirculation regions, whose effect becomes significant for $\Lambda_t > 10^{-2}$. These differences become smaller as Da increases. At very

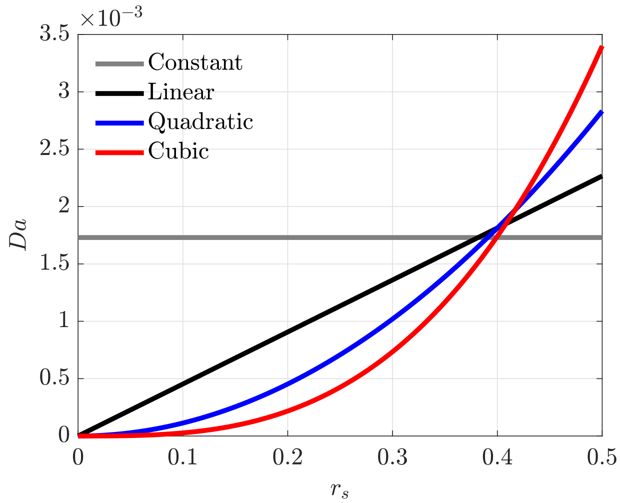

FIG. 13. Permeability as a function of the radius in spherical coordinates r_s for the distributions employed in the present analysis.

large permeabilities, an increase in slip leads to slightly larger recirculations.

These differences in the flow morphologies have a strong effect on the marginal stability curves, as shown in figure 11 for the steady mode and in figure 12 for the unsteady mode. Initially, the isotropic case is considered, i.e. $\Lambda_s = \Lambda_t$. The marginal stability curves with varying Λ_t follow the same trend. At low permeabilities, an increase in the slip leads to an increase in the critical Reynolds number, which becomes significant for $\Lambda_t > 10^{-2}$, the minimum values of Re_{cr} slightly increase and the critical permeability for unconditional stability with Re are not significantly influenced by variations of Λ_t. We then investigate the effect of anisotropy in the slip tensor, i.e. $\Lambda_t \neq \Lambda_s$. The results show that the increase in the critical Reynolds number is significant when large values of Λ_t, with $\Lambda_s = 0$, are considered, while a large value of Λ_s with $\Lambda_t = 0$ does not strongly influence the flow morphology. This behavior can be interpreted by considering that Λ_t influences both the baseflow and stability problems, while Λ_s affects only the stability problem. Very large values of Λ_t imply much smaller recirculation regions (for low permeabilities); therefore, the flow is stabilized owing to the reduction of the region in which the instability develops. Higher Reynolds numbers are thus needed to develop the instability, as shown in figures 11 and 12. These differences become smaller in the proximity of the minima of Re_{cr} and of the critical value of Da for unconditional stability.

The variation of the slip length leads to quantitative differences in the flow morphology and stability properties, with an overall reduction of the size of the recirculation region. However, the physics is dominated by the permeability. To deepen the role of the permeability in the flow dynamics and stability, the following section focuses on the effect of variable permeability distributions inside the body, always keeping the hypothesis of an isotropic porous medium.

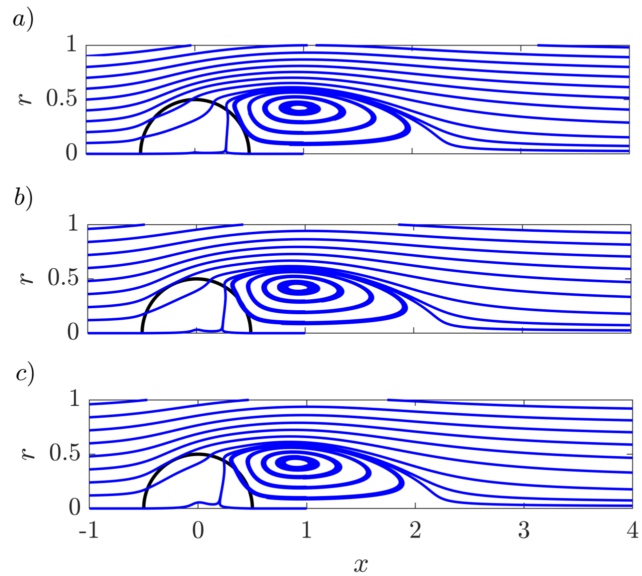

FIG. 14. Streamlines for $\overline{Da} = 1.7 \times 10^{-3}$, $\Lambda_t = 0$ and $Re = 150$, in the case of a) linear, b) quadratic and c) cubic distributions of permeability along r_s.

IV. WAKE FLOWS PAST SPHERES OF VARIABLE PERMEABILITY

The previous section studied the effect of permeability and slip (kept constant inside the porous medium) on the flow morphology past a permeable sphere. However, typical porous spheres may present variable distributions of permeability rather than a constant one. To give an example, the sea urchin can be seen as a porous structure with a solid core, whose inclusions are needles. Owing to the radial distribution of needles, the permeability increases while reaching the tip of the needles. In addition, many seeds are transported in the air by parachute-like structures, called pappi, composed of filaments that can be arranged in disk or spherical arrays that lead to non-constant permeability distributions.

Despite the increasing interest for these natural structures[15], systematic works on the stability properties in the case of variable permeability are still limited in the literature[16]. This section proposes a parametric study in which the permeability varies inside the sphere while always considering an isotropic porous medium, i.e. $\mathbf{Da} = Da(x,r)\mathbf{I}$. We neglect variations of the slip lengths ($\Lambda_t = \Lambda_s = 0$) since they do not qualitatively modify the flow features.

Three polynomial distributions of permeability, linear, quadratic and cubic, are considered. The outlined variations occur along the radius of the spherical reference frame $(r_s, \varphi_s, \theta_s = \theta)$ with origin the center of the sphere. A constant average value of the Darcy number, $\overline{Da}$, is imposed for each

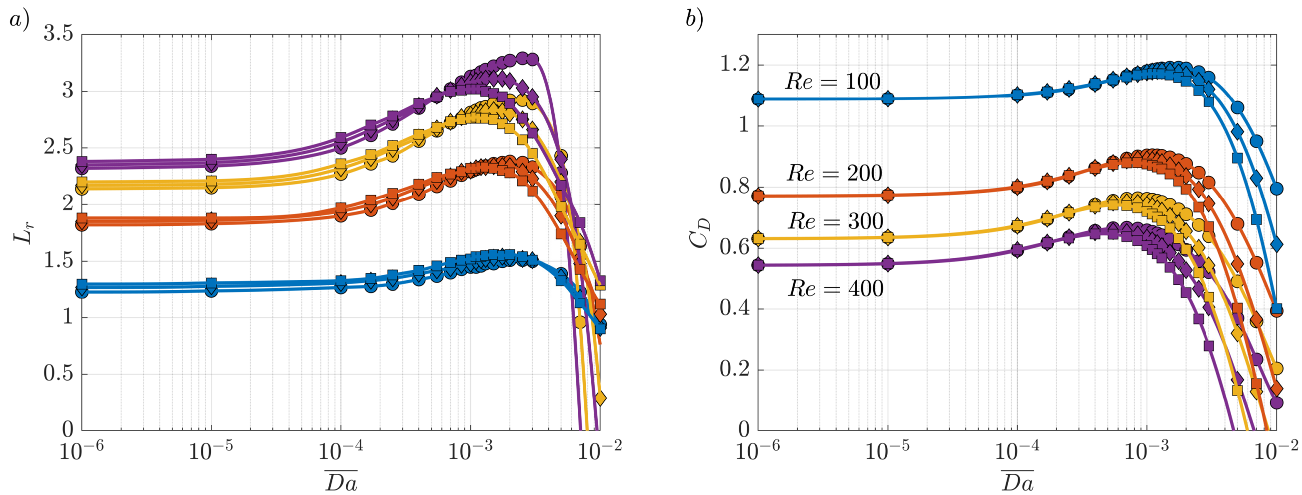

FIG. 15. *a*) Length of the recirculation region L_r and *b*) drag coefficient C_D as functions of $\overline{Da}$, in the absence of slip, for the linear (dots), quadratic (diamonds) and cubic (squares) distributions. The different clusters of curves refer to $Re = 100$ (blue), $Re = 200$ (orange), $Re = 300$ (yellow) and $Re = 400$ (purple).

case:

$$\overline{Da} = \frac{1}{V}\int_V Da(x,r)\,dV = \frac{6}{\pi}\int_0^{2\pi}\int_0^{\pi}\int_0^{0.5} Da(r_s) r_s^2 \sin\vartheta_s \mathrm{d}r_s \mathrm{d}\varphi_s \mathrm{d}\theta_s. \quad (26)$$

The different distributions as a function of $\overline{Da}$ are thus obtained:

- constant: $Da(r_s) = \overline{Da}$,
- linear: $Da(r_s) = \frac{8}{3}\overline{Da} r_s$,
- quadratic: $Da(r_s) = \frac{20}{3}\overline{Da} r_s^2$,
- cubic: $Da(r_s) = 16\overline{Da} r_s^3$.

For the sake of clarity, the notation $Da \propto r_s^\alpha$ is introduced, where $\alpha (= 0, 1, 2, 3)$ is the order of the polynomial distribution. Figure 13 shows the different distributions for $\overline{Da} = 1.7 \times 10^{-3}$. An increase in α leads to two effects. First, the permeability decreases close to the sphere center; second, higher values are reached in the proximity of the interface. These considerations will find an application in the following sections, which describe the baseflow and its stability properties.

A. Steady and axisymmetric flow

This section focuses on the effect of the permeability distribution on the steady and axisymmetric flow. In figure 14, a qualitative visualization with the flow streamlines is proposed, for $\overline{Da} = 1.7 \times 10^{-3}$. The flow morphology is not significantly affected, and a slight variation of the size of the recirculation region with α is observed. These slight differences are quantified in figure 15*a*, which shows the variation of the length of the recirculation region with $\overline{Da}$ and for different values of *Re*.

In all cases, we observe a behavior similar to the one with constant permeability. An initial increase of L_r is followed by a rapid decay at very large permeabilities. As α increases, the maximum L_r presents slightly larger values attained at smaller values of $\overline{Da}$. At very large permeabilities, the recirculation presents a slower decrease with $\overline{Da}$ as α increases, thus leading again to slightly larger recirculations.

The drag coefficient presents a similar behavior, as reported in figure 15*b*. Also in this case, the maximum is progressively anticipated as α increases. A slightly smaller maximum is attained for larger values of α.

These observations are explained by an observation of the distributions of permeability outlined in figure 13. The initial slightly higher values of L_r for linear, quadratic and cubic distributions are related to the increase of permeability close to the interface, for fixed $\overline{Da}$. In the constant permeability case, an increase of permeability leads to an increase in the size of the recirculation region, for small enough Da. The outlined phenomenon also appears in this case since the permeability close to the interface increases with α. We thus observe a slight increase in the length of the recirculation region and a displacement of the maximum at smaller values of $\overline{Da}$. Beyond the maximum, the slower decrease with α is related to the presence of a core close to the center of small permeability. As a consequence, the fluid is constrained to pass around and through a region of lower permeability. The rapid drop of L_r is thus reduced by the presence of this core of low permeability, which ensures the presence of larger recirculation regions. However, the drag coefficient presents a faster drop with α, at large permeabilities. Despite the presence of the core of low permeability, the pressure and velocity gradients at the interface are largely reduced, and thus the forces acting at the interface decrease.

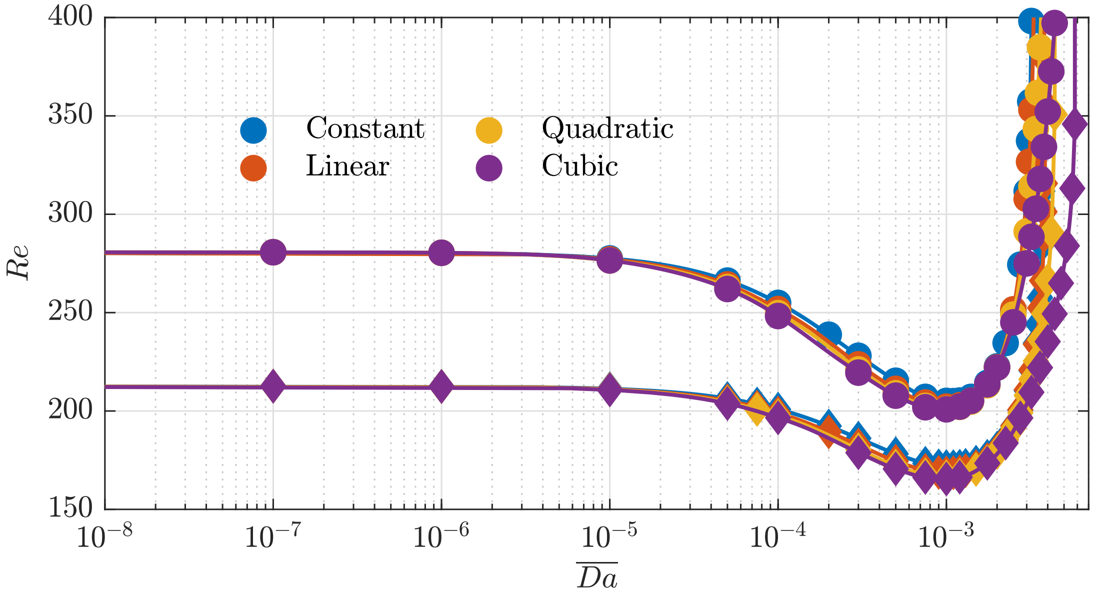

FIG. 16. Critical Reynolds number as a function of $\overline{Da}$, in the absence of slip, for different distributions of permeability, steady (diamonds) and unsteady (dots) bifurcations.

B. Stability with respect to azimuthal perturbations

In analogy with the constant permeability case, here we perform a stability analysis of the steady and axisymmetric wake for the different polynomial distributions. The results are reported in terms of marginal stability curves in figure 16. The first bifurcation is denoted with diamonds, while the second one with dots. The different colors correspond to the distributions employed in this work. Interestingly, the employment of the average permeability $\overline{Da}$ leads to a collapse of the marginal stability curves for the different distributions. In all cases, a minimum in the critical Reynolds numbers is attained, which slightly decreases employing polynomials of higher order, and a critical value of the permeability beyond which the wake is stable independently of *Re* is identified, which increases with α. Also these results can be correlated to the different distributions of permeability. The slight decrease in the critical Reynolds number is related to the increase of permeability at the interface which induces larger recirculations as polynomials of higher order are employed, since the stability properties are directly related to the extent of the recirculation regions. The increase in the critical *Da* with α is instead related to the core of low permeability, which ensures larger recirculations compared to the constant permeability case. Larger recirculations thus imply more unstable configurations, and the instability is moved at larger $\overline{Da}$.

To summarize, the flows and the stability properties are very similar when the same average value of the permeability, $\overline{Da}$, is considered. Moreover, the flow morphologies are weakly dependent on the employed distribution of permeability. The small differences were explained by recalling the constant permeability case and focusing on the (i) decrease of permeability close to the center and (ii) increase of the permeability at the body/fluid interface as α increases. The similarities in the flow morphology result in very similar stability properties at a given $\overline{Da}$.

So far, we have focused on a systematic study in which the permeability and the slip were considered as parameters. However, a remarkable peculiarity of the employed homogenized model is the direct link between the permeability and slip with the structure composing the porous body. While these techniques showed great potential in their employment in the case of simple periodic arrays, applications to more elaborate geometries are still lacking. Henceforth, we aim at retrieving the full-scale structure for a constant permeability in the local spherical reference frame, thus giving an example of how to close the link between porous models and the micro-structure of the porous body itself for a three-dimensional configuration of interest. The inversion of the classical paradigm "from geometry to macroscopic properties" can be of paramount importance in multiple scales structures design, as shown in Schulze and Sesterhenn[76] and Ledda et al.[66]. Several benefits can be obtained by identifying the desired permeability distribution through the homogenized model and then retrieving the full-scale structure by an inverse design that satisfies the macroscopic properties. There is an infinity of possible geometries with the same macroscopic properties, giving great potential to this inverse paradigm in terms of reduction of computational costs and in the possibility to explore different configurations[66]. In the considered case, different choices for the full-scale structures could be employed, e.g. arrays of cylinders propagating radially from the center or arrays of packed spheres. In this work, we consider a configuration that allows to directly study the full-scale structure with the axisymmetric Navier-Stokes equations, i.e. an array of concentric rings. Using this particular scaffold, we develop a procedure to obtain the geometrical details (the radius and position of the rings) starting from the macroscopic

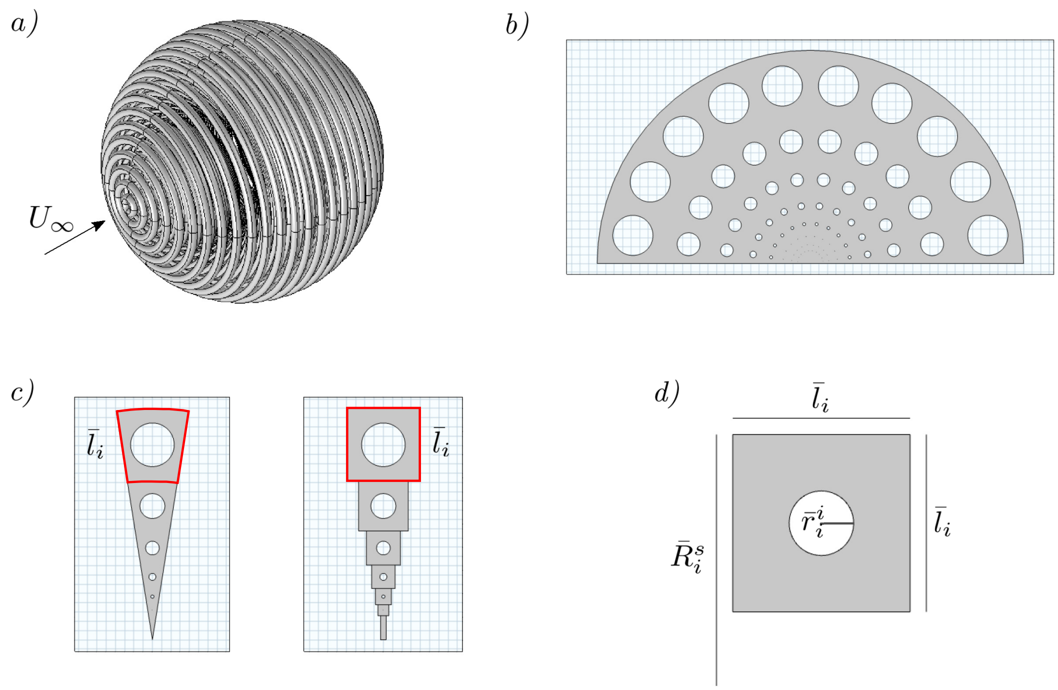

FIG. 17. a) Sketch of the three-dimensional structure of the sphere. b) Fluid domain internal to the sphere and distribution of rings at one azimuthal section. c) Sketch of the geometrical approximation for each polar repetition which leads to an array of square elementary volumes. d) Resulting elementary volume for the evaluation of the local permeability, highlighted in red in c).

properties of the permeable sphere. However, similar procedures can be developed for different full-scale structures.

V. DESIGN OF A SPHERE OF CONSTANT PERMEABILITY: CONCENTRIC RINGS

A. Design procedure

The permeable sphere is composed of an array of toroidal fibers with circular cross-sections, oriented such that the rings axes are coincident with the $r = 0$ axis of the cylindrical reference system, see figure 17a. The flow is axisymmetric when the array is invested by a uniform stream along the axial direction and thus solved in one azimuthal cross-section. In the azimuthal cross-section $\theta = 0$, the rings are disposed with polar symmetry and are represented by circular inclusions (see figure 17b, where the fluid region inside the sphere is represented in grey). The procedure consists in the determination of the radius of each ring composing the sphere to obtain the desired distribution of Da. In principle, the radius of each inclusion can be arbitrarily varied to obtain a desired distribution of permeability, as explained next. Since in the previous section we have shown that permeability variations along the radius do not qualitatively change the flow phenomenology and stability properties of the wake, we focus on a constant distribution of permeability. Therefore, the first input parameter of the procedure is the bulk Darcy number Da. A structure composed of N polar repetitions of the element is adopted, sketched in the left frame of figure 17c. Each polar element can be divided in curved elementary cells of characteristic size $\bar{l}_i$ (cf. left frame of figure 17c). The procedure to retrieve the full-scale structure is based on the knowledge of the separation of scales parameters of the interface cell of the periodic repetition $\varepsilon = \varepsilon_1$ (cf. the cell highlighted in red in figure 17c). With the initial definition of ε and Da, the micro-structure is uniquely determined. We now outline the assumptions of the procedure to determine the radii of the rings. We assume $\bar{l}_i \ll \bar{R}_c$, where $\bar{R}_c$ is the local spherical radius. Under this assumption, the curvature of each elementary cell is neglected, implying that the rings can be considered as three-dimensional cylinders. Owing to the azimuthal invariance, we can consider the two-dimensional problem at a fixed azimuthal section and thus each polar repetition can be decomposed in square elementary cells, each containing a single circular inclusion (cf. right frame of figure 17c). Neglecting the curvature in the azimuthal direction for the same reason, and assessing the invariance of the geometry along the same direction, two-dimensional cells can be finally adopted as microscopic domain. Note that these assumptions are reasonably respected at the interface, while they do not hold close to the center of the sphere. However, the effect on the results of a core of low permeability is weak and manifests itself only at very large permeabilities, as previously shown. The last assumption is equivalent to state that the variations of the micro-structure are sufficiently smooth to consider each cell as a periodic repetition. As will become clear once outlined the procedure, this assumption is respected provided that there

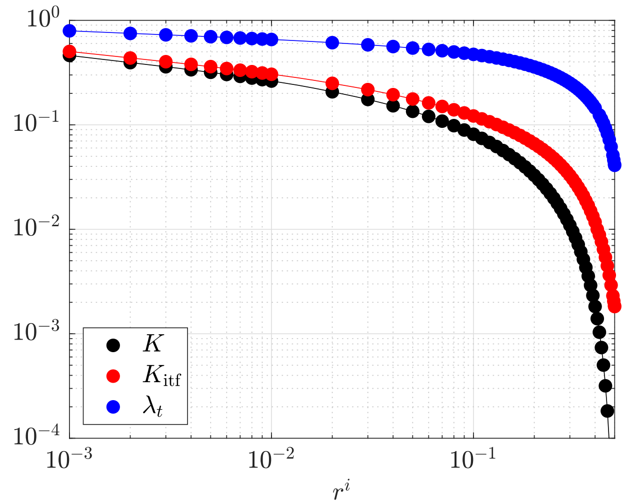

FIG. 18. Variation of the permeability K, the interface permeability $K_{\rm itf}$, and the slip length λ_t with the radius r^i, for circular inclusions in a square domain.

is sufficient separation of scales for each cell:

$$\varepsilon_i = \bar{l}_i/D \ll 1. \tag{27}$$

The problem is thus simplified by considering two-dimensional elementary cells of different sizes and inclusion radii, whose macroscopic properties (permeability, interface permeability, and slip) are given by simulations with periodic conditions. We now outline the complete procedure, from the determination of the properties of the considered microscopic geometries to the final macro-structure. We can distinguish three different steps, (i) the determination of the properties of the considered micro-structure, i.e. circular inclusions with different radii, (ii) the determination of the distribution and size of the elementary cells composing the porous structure with input ε, and (iii) the determination of the circular inclusions radii with input Da.

The elementary unit-cell characterizing the porous structure is sketched in figure 17*d*. The method outlined in Naqvi and Bottaro[68] is exploited to evaluate the permeability, interface permeability, and slip number. The microscopic problems are solved by non-dimensionalizing them with the characteristic microscopic length $\bar{l}_i$. With this precaution, the permeability $\mathbf{K} = K\mathbf{I}$, the interface permeability $\mathbf{K}_{\rm int} = K_{\rm int}\mathbf{I}$ and slip λ_t, normalized with respect to the characteristic length of the square elementary cell $\bar{l}_i$, are evaluated by considering a two-dimensional array of inclusions and plotted as a function of the inclusion radius r^i. We refer to Appendix B for further detail about the computations. The results, non-dimensionalized with the microscopic length, are reported in figure 18, in the range $10^{-3} < r^i < 0.49$. All quantities diverge as the inclusion radius goes to zero, while they tend to zero as the radius of the solid inclusion reaches $r^i = 0.5$. The cells in figure 17*c* are labeled with the index $i = 1, 2, \ldots$, increasing from the interface to the center. Each i-th cell is characterized by its arc length on the top boundary of the cell, equal to the radial dimension, $\bar{l}_i$, the radius of the solid inclusion $\bar{r}^i_i$, and the local spherical radius at the top boundary of the cell $\bar{R}^s_i$.

The input separation of scales parameter at the interface elementary cell $\varepsilon = \varepsilon_1$ is used to determine the angular distance between two polar repetitions:

$$\Delta\varphi = \frac{2\pi}{N} = \frac{2\bar{l}_1}{\hat{D}} = 2\varepsilon. \tag{28}$$

The size ε_{i+1} and radial position R^s_{i+1} of the $(i+1)$th elementary cell of the cross-section are determined via the following recursive relations:

$$R^s_{i+1} = R^s_i - \bar{l}_i/D = R^s_i - \varepsilon_i, \tag{29}$$

$$\varepsilon_{i+1} = \tfrac{2\pi}{N}\left(R^s_i - \varepsilon_i\right), \tag{30}$$

which are non-dimensionalized with the diameter of the sphere. The initial step is given by the external elementary cell ($R^s_1 = 0.5$) with the input separation of scales parameter $\varepsilon_1 = \varepsilon$. The recursive algorithm is stopped at the index $i-1$ such that $R^s_i < 0.05$ to avoid extremely small inclusions, i.e. approximately less than 10^{-6} times the sphere radius.

Once the size and position of the elementary cells (each one assumed to be square, cf. left frame of figure 17*c*) is determined, one should define the radius of the microscopic inclusions inside each elementary cell. A constant value of Da is thus imposed by exploiting the results of the microscopic simulations shown in figure 18, in which the microscopic radius is related to the permeability K. In each cell of size ε_i, the permeability K_i is given by:

$$K_i\left(r^i_i\right) = Da/\varepsilon_i^2. \tag{31}$$

Exploiting the bijective relation between r^i_i and K_i (cf. figure 18), the radius r^i_i of the inclusions in each elementary cell is thus determined.

For the analysis of the permeable sphere with the homogenized model two additional parameters are needed, i.e. the slip length and the interface Darcy number. At this stage, one could modify the radius of the inclusion close to the interface to obtain the desired values of interface permeability and slip. To avoid further complications in the design procedure, the interface permeability and slip are *a posteriori* evaluated without modifying the microscopic inclusion at the interface:

$$\Lambda_t = \varepsilon_1 \lambda_t\left(r^i_1\right), \tag{32}$$

$$Da_{\rm int} = \varepsilon_1^2 K_{\rm int} = \varepsilon_1^2 K_{\rm int}\left(r^i_1\right), \tag{33}$$

The geometry of the sphere and its properties are now uniquely determined for a given value of Da and ε. In the following, the results given by the full-scale simulations are compared with the homogenized model where Da, $Da_{\rm int}$ and Λ_t are provided.

B. Comparison with the homogenized model

We conclude the analysis by comparing some full-scale simulations (FSS) with the homogenized model (HM) for different permeability values. By FSS, we intend simulations

Case	N	ε	Da	Da_{int}	Λ_t
I	14	0.22	1.7×10^{-3}	3.2×10^{-3}	0.079
II	30	0.11	5×10^{-4}	10^{-3}	0.044
III	60	0.05	10^{-5}	4.3×10^{-5}	0.009

TABLE I. Values of the geometrical parameters and homogenized properties for each case.

	FSS(I)	HM(I)	FSS(II)	HM(II)	FSS(III)	HM(III)
L_r	1.24	1.42	1.36	1.46	1.48	1.5
C_D	0.76	0.80	0.82	0.89	0.86	0.87

TABLE II. Comparison between the full-scale simulations (FSS) and the homogenized model (HM) for the three outlined cases.

that explicitly account for the micro-structure composing the sphere. Such simulations are computationally expensive owing to the scale separation between the macroscopic diameter and the typical micro-structure size l_i. The purpose of the comparison carried out in the present section is to appraise the accuracy of the much simpler model obtained by homogenization. The following three cases, summarized in table I, are considered:

- Case I, characterized by $N = 14$ polar repetitions and $Da = 1.7\times10^{-3}$.
- Case II, characterized by $N = 30$ polar repetitions and $Da = 5\times10^{-4}$.
- Case III, characterized by $N = 60$ polar repetitions and $Da = 10^{-5}$.

The FSS results are compared to those of the HM. The Reynolds number is fixed to $Re = 150$, less than the minimum value of Re_{cr} to ensure the linear stability of the FSS and HM solutions. Table II shows the results in terms of length of the recirculation region and drag coefficient for the three different cases introduced above. The accuracy of the HM is $\mathscr{O}(\varepsilon)$ as predicted by the homogenization theory. In particular, the HM is progressively more accurate as ε decreases; at the same time, while the computational cost of the HM is constant with ε, the FSS are progressively more CPU-demanding as ε decreases.

In figure 19 the flow streamlines are qualitatively compared. The flow morphology is well reproduced, in particular when the separation of scales increases. Surprisingly, there is a qualitative agreement even in Case I, for which the separation of scales parameter $\varepsilon = 0.22$ is relatively large and thus violates the hypothesis $\varepsilon \ll 1$. Figure 20 shows a final quantitative comparison, in which the axial velocity profiles at $x = 0.0175$ well agree, for Cases II and III.

Despite the numerous assumptions made to exploit the two-dimensional HM results for the case of a three-dimensional sphere, the FSS well agree with the HM. Therefore, the HM is suitable even for complex flows such as the one outlined in the present work. The flow morphologies outlined in the parametric studies of Sections III and IV were recovered, thus showing the great potential of the homogenization technique in predicting wake flows via simple equations and boundary

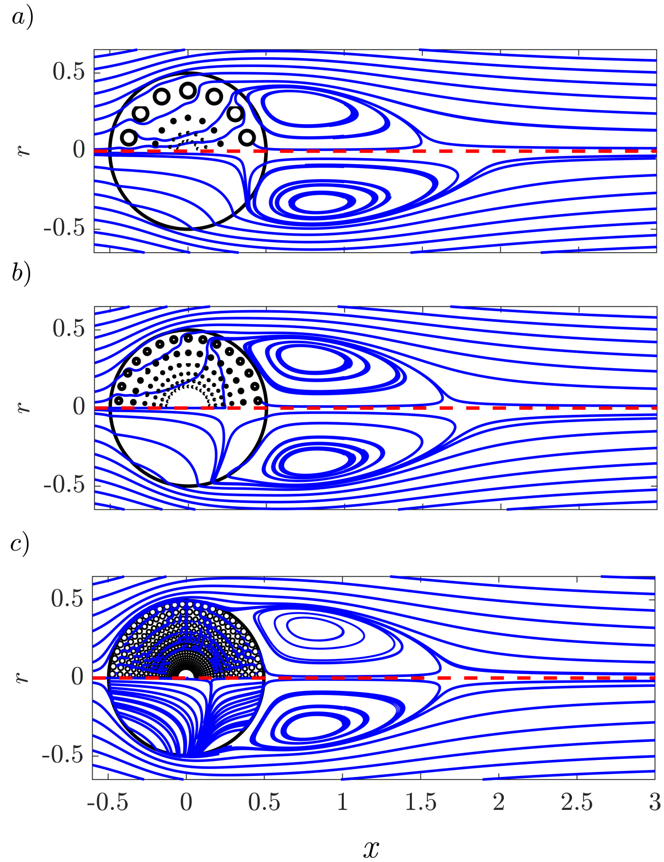

FIG. 19. Comparison of the flow streamlines between the full-scale simulation (on the top) and homogenized model (on the bottom), *a*) Case I, *b*) Case II, *c*) Case III.

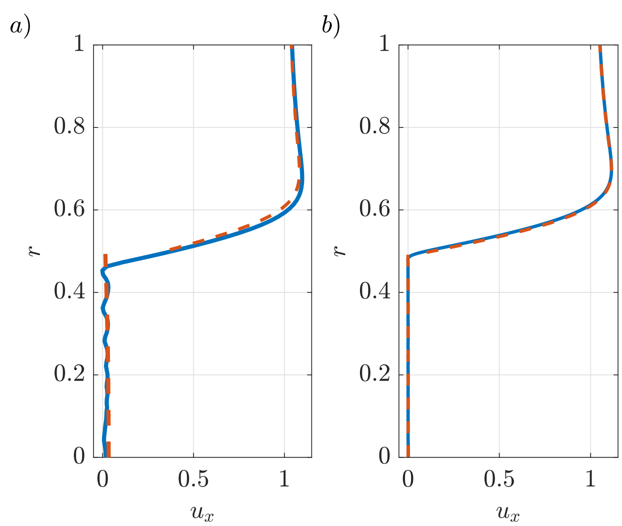

FIG. 20. Streamwise velocity profile at $x = 0.0175$, homogenized model results (orange dashed lines) and full-scale simulations (blue lines), for Cases *a*) II and *b*) III.

conditions, and in reproducing actual wake structures downstream the considered bluff body.

VI. CONCLUSIONS

In this work, we studied the morphology and stability properties of the steady and axisymmetric flow past a permeable sphere. A homogenized model was employed, consisting in the Darcy law inside the porous medium, with a slip condition on the tangential velocity at the interface between the fluid and porous region. The main character in the Darcy model is the permeability, which quantifies the resistance for the fluid to pass through the micro-structure. The slip length appears in the interface condition as well and accounts for the viscous effects in the proximity of the interface. The initial part of the work was devoted to the steady and axisymmetric flow in the presence of a constant and isotropic permeability and zero slip length. The flow presents a penetration of the recirculation region inside the sphere, which increases its dimensions as the permeability increases, as already observed in Yu et al.[49], where a different porous model was employed. However, at very large permeabilities, the recirculation region leaves the body, moves downstream, and eventually disappears. The non-monotonous behavior of the recirculation region resulted in a particular behavior of the marginal stability curves for the two bifurcations of the steady and axisymmetric wake. The critical Reynolds numbers for the instability reached a minimum, much lower than the ones of the solid case, and then drastically increased for very large permeabilities. A critical permeability was identified, beyond which the steady and axisymmetric wake is linearly stable independently of the Reynolds number. A consequent analysis showed that the slip length weakly influences the flow morphology. Therefore, the latter is largely affected by the permeability.

We then focused on the effect of various polynomial distributions of permeability along the spherical radial direction r_s, i.e. proportional to r_s^α, still under the assumption of an isotropic porous media. The results showed a similar behavior to the case of constant permeability, with only slight differences. Interestingly, the flow morphologies and stability curves collapse when an average permeability is employed, thus highlighting the secondary role of the spatial distribution of permeability for the considered cases.

While in the previous sections the permeability and slip length were treated as free parameters, in the last section these properties were linked with an actual porous structure. The homogenization theory enabled us to retrieve an actual permeable sphere through some reasonable assumptions. We showed the potential of homogenization theory in the modelization of actual three-dimensional configurations of interest by comparing the homogenized model against the reference cases obtained by full-scale simulations.

This work provides an example of the application of the porous homogenized model with slip to a three-dimensional configuration of interest, together with the characterization of the effect of a penetrating recirculation region on the steady and axisymmetric flow past a permeable sphere, with a focus on its stability properties. In opposition to other bluff body wakes, a remarkable and counterintuitive effect is the decrease of the critical Reynolds number for the marginal stability. The homogenized model was applied to a three-dimensional configuration of interest. Thanks to the direct link with the actual full-scale structure, we showed the potential of the inverse procedure to retrieve the geometry starting from the homogenized parameters. These considerations may find application in the optimization and design of porous structures, not only in aerodynamic flows. The inverse paradigm can significantly decrease the computational effort needed for optimization procedures since (i) the homogenized model contains only few parameters, which describe the macroscopic effect of the microscopic geometry, that can eventually vary in space[66], with great advantage compared to the large numbers of degrees of freedom needed to optimize a micro-structured medium, and (ii) the decoupling between macroscopic effect and microscopic structure design helps in considering different structures without loss of generality. These results can be extended in several ways. While detached recirculation regions are receiving growing attention, further developments may include the analyses of penetrating recirculation regions for different flow configurations. These findings can be applied in classical environmental studies such as porous particle or seed transport[15,16] or in chemical engineering processes which involve the presence and settling of spherical, porous particle clusters[23,25,77]. In this work, we characterized the two bifurcations of the steady and axisymmetric wake. Further developments may include the non-linear interactions of these two modes varying the permeability and slip length and the secondary instability of the steady non-axisymmetric bifurcated state. Finally, we retrieved the full-scale structure by exploiting the homogenization theory developed for the two-dimensional case. A natural extension of this theory to cylindrical and spherical coordinates would give access to a broader range of geometries and applications.

ACKNOWLEDGMENTS

We acknowledge the financial support of the Swiss National Science Foundation (grant no.200021_178971 to P.G.L. and grant no. 514636 to G.A.Z). F.G. and G.A.Z. acknowledge the EuroTech Postdoc Programme, co-funded by the European Commission under its framework programme Horizon 2020, (grant agreement no. 754462).

AUTHOR DECLARATIONS

Conflict of Interests

The authors declare no conflict of interest.

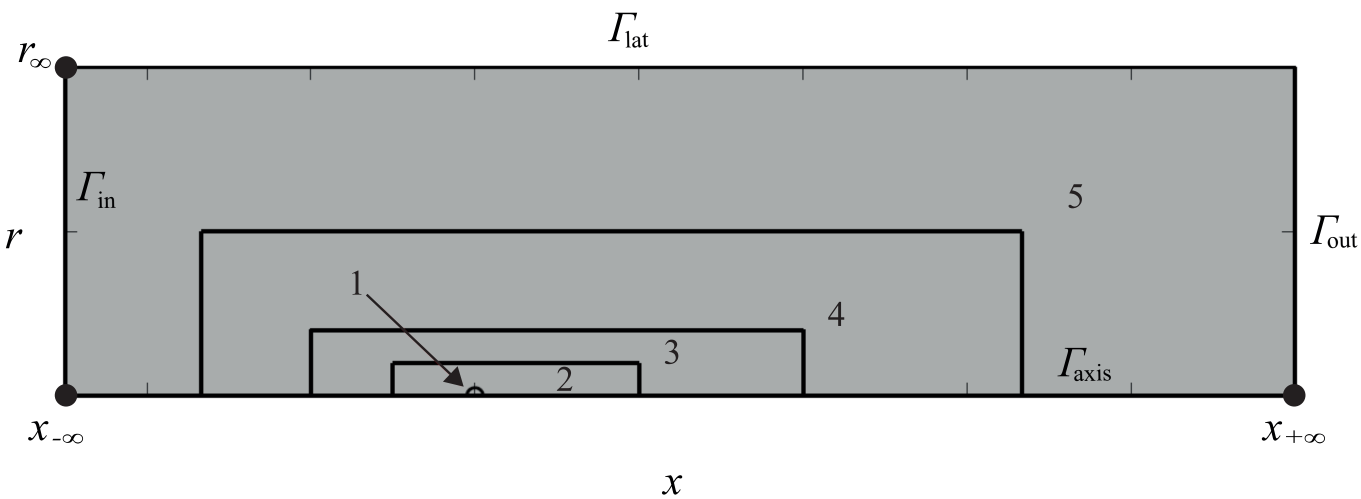

FIG. 21. Sketch of the refinement regions of the computational domain.

Mesh	$x_{-\infty}$	$x_{+\infty}$	r_∞	n_c	n_2	n_3	n_4	n_5	N_{tot}
M1	−50	100	40	200	15	6.25	2	1.5	334534
M2	−37.5	75	30	200	15	6.25	2	1.5	222393
M3	−30	60	24	200	15	6.25	2	1.5	169039
M4	−25	50	20	200	15	6.25	2	1.5	136696
M5	−25	50	20	220	22.5	7.5	2.5	1.75	158954
M6	−25	50	20	240	27.5	7.5	2.5	1.75	213713
M7	−25	50	20	260	30	7.5	3	2	274383

TABLE III. Different meshes employed for the validation procedure. The upstream and downstream location of the domain boundaries are denoted $x_{-\infty}$ and $x_{+\infty}$, respectively, the radial size as r_∞, n_c is the number of vertices at the interface, while n_2, n_3, n_4 and n_5 are the vertex densities on the external sides of the corresponding refinement regions; N_{tot} is the total number of elements.

DATA AVAILABILITY

The data which support this study are available from the corresponding author upon reasonable request.

Appendix A: Numerical validation

	$Da = 0.0036$		$Da = 0.0032$	
Mesh	σ_1	C_D	σ_2	C_D
M1	-0.0035510	0.6255	$-0.0013298+0.30833i$	0.63275
M2	-0.0035462	0.62558	$-0.0013150+0.30835i$	0.63277
M3	-0.0035322	0.62560	$-0.0012567+0.30839i$	0.63280
M4	-0.0035178	0.62562	$-0.0012567+0.30839i$	0.63282
M5	-0.0034105	0.62594	$-0.0011703+0.30847i$	0.63311
M6	-0.0033208	0.62618	$-0.0011307+0.30853i$	0.63335
M7	-0.0032129	0.62637	$-0.0010653+0.30860i$	0.63354

TABLE IV. Results of the validation procedure for $Re = 390$, with $Da = 0.0036$ (for the steady mode) and $Da = 0.0032$ (for the unsteady mode). We also report the values of the drag coefficient for the corresponding baseflows.

	$Da = 0.0037$		$Da = 0.0031$	
Mesh	σ_1	C_D	σ_2	C_D
M1	8.3077×10^{-4}	0.67046	$-0.0042442+0.34859i$	0.68891
M2	8.3525×10^{-4}	0.67047	$-0.0042320+0.34860i$	0.68893
M3	8.4511×10^{-4}	0.67050	$-0.0042127+0.34862i$	0.68896
M4	8.5985×10^{-4}	0.67053	$-0.0041836+0.34864i$	0.68899
M5	9.0638×10^{-4}	0.67078	$-0.0041290+0.34867i$	0.68921
M6	9.3256×10^{-4}	0.67098	$-0.0041154+0.34869i$	0.68940
M7	9.7854×10^{-4}	0.67113	$-0.0040814+0.34872i$	0.68954

TABLE V. Results of the validation procedure for $Re = 330$, with $Da = 0.0037$ (for the steady mode) and $Da = 0.0031$ (for the unsteady mode). We also report the values of the drag coefficient for the corresponding baseflows.

In this section, the mesh validation procedure is outlined. The computational domain is sketched in figure 21. The extension of the computational domain is from $x = x_{-\infty}$ to $x = x_{+\infty}$ along the x direction and from $r = 0$ (i.e. the symmetry axis) to $r = r_\infty$ along the radial direction. The sphere center is at the origin of the reference system. Five refinement regions are present, labeled with integers from 1 to 5, starting from inside the sphere and moving outward. The mesh is composed of triangular elements. Table III shows the different meshes considered for the validation.

We consider four different cases, in the vicinity of the marginal stability curves. We verify the convergence of drag coefficient and eigenvalues:

1. Re=390 and:
   - $a)$ $Da = 0.0032$ for the unsteady bifurcation;
   - $b)$ $Da = 0.0036$ for the steady bifurcation;
2. Re=330 and:
   - $a)$ $Da = 0.0031$ for the unsteady bifurcation.
   - $b)$ $Da = 0.0037$ for the steady bifurcation;

To verify the eigenvalues and C_D convergences, we vary (i) the domain size and (ii) the mesh resolution. Starting from Mesh M4 (table III), we progressively increase the domain size (meshes M3,M2 and M1). We then increase the mesh resolution with meshes M5,M6 and M7. The eigenvalues and drag coefficient for the different cases are reported in tables IV,V. In overall, the relative error on the drag coefficient is always less than 1%. The relative error on the eigenvalues is approximately constant for all cases and $\sim 10\%$. To have a clear picture of the expected accuracy in terms of critical Reynolds number, we evaluate Re_{cr} with meshes M4 and M7 in the vicinity of the considered cases (with fixed Da) :

- for case $1a$), the critical Reynolds numbers for the unsteady bifurcation at $Da = 0.0032$ read $Re_{cr}^{M4} = 398.22$ and $Re_{cr}^{M7} = 396.63$ for meshes M4 and M7, respectively, leading to an error of $\Delta Re_{cr} = 1.58$.

- for case $1b$), the critical Reynolds numbers for the steady bifurcation at $Da = 0.0036$ read $Re_{cr}^{M4} = 383.54$ and $Re_{cr}^{M7} = 384.07$ for meshes M4 and M7, respectively, leading to an error of $\Delta Re_{cr} = 0.53$.

- for case $2a$), the critical Reynolds numbers for the unsteady bifurcation at $Da = 0.0031$ read $Re_{cr}^{M4} = 337.32$ and $Re_{cr}^{M7} = 337.13$ for meshes M4 and M7, respectively, leading to an error of $\Delta Re_{cr} = 0.19$.

For case $2b$), we evaluate the variation of the critical Darcy number in the vicinity of the value for unconditional stability, with fixed $Re = 330$. The critical values read $Da_{cr}^{M4} = 0.003706$ and $Da_{cr}^{M4} = 0.003707$.

The error on the critical Reynolds number increases with Re itself and is, at most, of order $\Delta Re_{cr} \approx 1.6$, and the associated maximum relative error is $\approx 0.4\%$. Also, the precision on the critical Darcy number appears to be satisfactory. Therefore, we conclude that mesh M4 is a good compromise between the accuracy and the computational times for the large parametric study considered, which involves five different parameters (Re,Da, Λ_t, Λ_s, α), with a relative error less than 1% on the critical Reynolds numbers.

Appendix B: Evaluation of permeability and slip via homogenization theory

Several recent works based on multi-scale homogenization aimed at linking the microscopic structure of a porous medium to its macroscopic feedback on the surrounding flow, i.e. the bulk permeability and slip interface effects[62,64,65,67]. In these works, the microscopic structure is assumed to be periodic within the porous medium so that the bulk permeability can be calculated once for all in a periodic microscopic elementary cell. Additionally, an interface microscopic cell containing few inclusions across the fluid-porous boundary can be identified where some microscopic problems can be solved to retrieve the interface permeability and slip. In particular, Bottaro[67] and Naqvi and Bottaro[68] have shown that both bulk and interface macroscopic properties can be deduced from a unique interfacial microscopic problem, provided that the normal-to-the-interface size of the microscopic domain is large enough. Adopting this last development, all macroscopic quantities can be retrieved by the solution of the two sets of equations. We introduce the two-dimensional local reference frame (x_n, x_t), where n and t denote the normal and tangent directions to the interface, respectively. The microscopic problems to be solved involve the tensor quantities $\lambda_{ij}^{\dagger}$, $\kappa_{ij}^{\dagger}$ and the vector quantities $\xi_j^{\dagger}$ and $\chi_j^{\dagger}$, where $i, j = n, t$. The equations, written in components for the sake of clarity, read:

$$\frac{\partial \lambda_{ij}^{\dagger}}{\partial x_i} = 0, \quad -\frac{\partial \xi_j^{\dagger}}{\partial x_i} + \frac{\partial^2 \lambda_{ij}^{\dagger}}{\partial x_l^2} = 0, \tag{B1}$$

$$\lim_{x_n \to +\infty} \frac{\partial \lambda_{ij}^{\dagger}}{\partial x_n} = \delta_{ij}, \quad \lim_{y \to +\infty} \xi_j^{\dagger} = 0,$$

and

$$\frac{\partial \kappa_{ij}^{\dagger}}{\partial x_i} = 0, -\frac{\partial \chi_j^{\dagger}}{\partial x_i} + \frac{\partial^2 \kappa_{ij}^{\dagger}}{\partial x_k^2} = \delta_{ij} H(-x_n), \tag{B2}$$

$$\lim_{x_n \to +\infty} \frac{\partial \kappa_{ij}^{\dagger}}{\partial x_n} = 0, \quad \lim_{x_n \to +\infty} \chi_j^{\dagger} = 0,$$

where H is the Heaviside function centered in $x_n = 0$, corresponding to the starting point of the first interface unit cell. The macroscopic quantities used in the interface conditions (15) can be then retrieved by the solutions of problems (B1,B2) introducing the following relations

$$\lambda_t = \int_0^1 \lambda_{tt}^{\dagger}(x_n \to +\infty)\,\mathrm{d}t - x_n, \quad K_{\text{int}} = \int_0^1 \kappa_{tt}^{\dagger}(x_n \to +\infty)\,\mathrm{d}t \tag{B3}$$

and

$$K = \int_0^1 \kappa_{nn}^{\dagger}(x_n \to +\infty)\,\mathrm{d}t. \tag{B4}$$

The solution for $\lambda_{tt}^{\dagger}$, $\kappa_{nn}^{\dagger}$ and $\kappa_{tt}^{\dagger}$ is represented in the microscopic interface cell in figure 22 for a periodic array of cylinders of radius equal to 0.4. Once the average values of the microscopic quantities are evaluated using equations (B3,B4), upon rescaling with the macroscopic length, they can be used in equations (2) and (3) to establish a link between the microscopic structure and the corresponding macroscopic flow field.

[1] J. Finnigan, "Turbulence in plant canopies," Annual Review of Fluid Mechanics **32**, 519–571 (2000).

[2] H. M. Nepf, "Flow and transport in regions with aquatic vegetation," Annual Review of Fluid Mechanics **44**, 123–142 (2012).

[3] Y. Brunet, "Turbulent flow in plant canopies: historical perspective and overview," Boundary-Layer Meteorology **177**, 315–364 (2020).

[4] H. M. Nepf, "Drag, turbulence, and diffusion in flow through emergent vegetation," Water Resources Research **35**, 479–489 (1999).

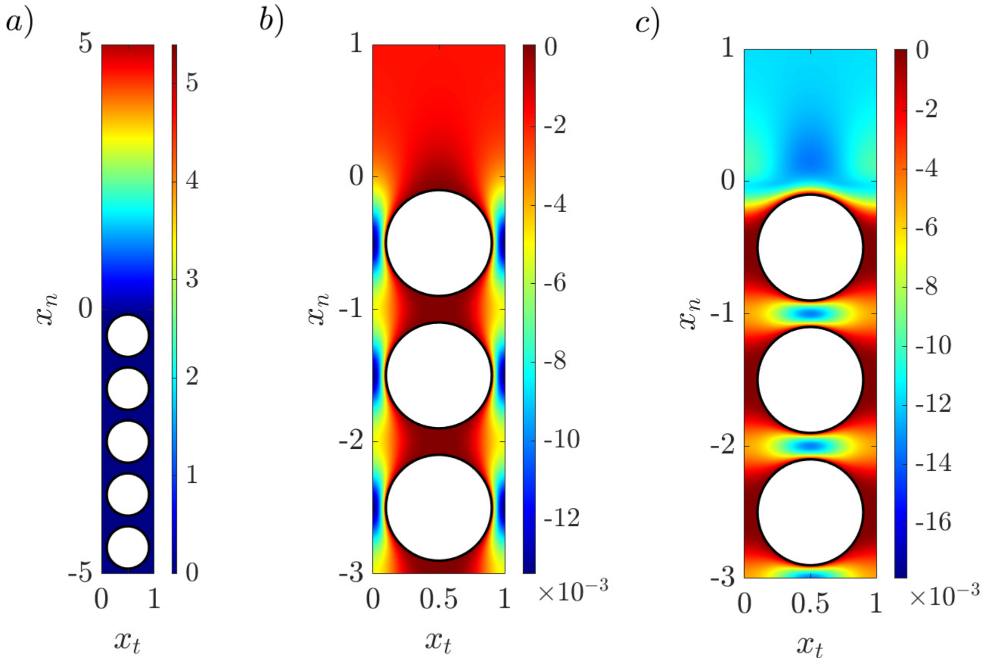

FIG. 22. Overview of the microscopic solution in the interface cell for a given circular inclusion whose radius is 0.4. *a*) $\lambda_{tt}^{\dagger}$ in the whole interface cell. *b*),*c*) Zoom in on the first three solid inclusions in the interface cell for *b*) $\kappa_{nn}^{\dagger}$ and *c*) $\kappa_{tt}^{\dagger}$.

[5] E. de Langre, "Effects of wind on plants," Annual Review of Fluid Mechanics **40**, 141–168 (2008).

[6] I. Battiato and S. Rubol, "Single-parameter model of vegetated aquatic flows," Water Resources Research **50**, 6358–6369 (2014).

[7] G. Zampogna, F. Pluvinage, A. Kourta, and A. Bottaro, "Instability of canopy flows," Water Resources Research **52**, 5421–5432 (2016).

[8] A. M. Hamed, A. M. Peterlein, and I. Speck, "Characteristics of the turbulent flow within short canopy gaps," Physical Review Fluids **5**, 123801 (2020).

[9] A. Sharma and R. García-Mayoral, "Turbulent flows over dense filament canopies," Journal of Fluid Mechanics **888** (2020).

[10] S. Endrikat, D. Modesti, R. García-Mayoral, N. Hutchins, and D. Chung, "Influence of riblet shapes on the occurrence of kelvin–helmholtz rollers," Journal of Fluid Mechanics **913** (2021).

[11] M. Liu, W. Huai, and B. Ji, "Characteristics of the flow structures through and around a submerged canopy patch," Physics of Fluids **33**, 035144 (2021).

[12] C. Y. Wong, P. H. Trinh, and S. J. Chapman, "Shear-induced instabilities of flows through submerged vegetation," Journal of Fluid Mechanics **891** (2020).

[13] H. Wagner, M. Weger, M. Klaas, and W. Schröder, "Features of owl wings that promote silent flight," Interface Focus **7**, 20160078 (2017).

[14] J. Jaworski and N. Peake, "Aeroacoustics of silent owl flight," Annual Review of Fluid Mechanics **52**, 395–420 (2020).

[15] C. Cummins, M. Seale, A. Macente, D. Certini, E. Mastropaolo, I. Viola, and N. Nakayama, "A separated vortex ring underlies the flight of the dandelion," Nature **562**, 414–418 (2018).

[16] P. G. Ledda, L. Siconolfi, F. Viola, S. Camarri, and F. Gallaire, "Flow dynamics of a dandelion pappus: A linear stability approach," Phys. Rev. Fluids **4**, 071901 (2019).

[17] F.-S. Qiu, T.-B. He, and W.-Y. Bao, "Effect of porosity on separated vortex rings of dandelion seeds," Physics of Fluids **32**, 113104 (2020).

[18] M. A. Shannon, P. W. Bohn, M. Elimelech, J. G. Georgiadis, B. J. Mariñas, and A. M. Mayes, "Science and technology for water purification in the coming decades," Nature **452**, 301–310 (2008).

[19] A. Rahardianto, B. C. McCool, and Y. Cohen, "Accelerated desupersaturation of reverse osmosis concentrate by chemically-enhanced seeded precipitation," Desalin. **264**, 256–267 (2010).

[20] J. Olivier, "Fog harvesting: An alternative source of water supply on the West Coast of South Africa," GeoJournal **61**, 203–214 (2004).

[21] R. Labbé and C. Duprat, "Capturing aerosol droplets with fibers," Soft Matter **15**, 6946–6951 (2019).

[22] P. Levresse, I. Manas-Zloczower, D. Feke, Y. Bomal, and D. Bortzmeyer, "Observation and analysis of the infiltration of liquid polymers into calcium carbonate agglomerates," Powder Technology **106**, 62–70 (1999).

[23] P. Levresse, I. Manas-Zloczower, and D. Feke, "Hydrodynamic analysis of porous spheres with infiltrated peripheral shells in linear flow fields," Chemical engineering science **56**, 3211–3220 (2001).

[24] A. Bhattacharyya, "Effect of momentum transfer condition at the interface of a model of creeping flow past a spherical permeable aggregate," European Journal of Mechanics-B/Fluids **29**, 285–294 (2010).

[25] J. H. Masliyah and M. Polikar, "Terminal velocity of porous spheres," The Canadian Journal of Chemical Engineering **58**, 299–302 (1980).

[26] V. Patwardhan and C. Tien, "Sedimentation and liquid fluidization of solid particles of different sizes and densities," Chemical Engineering Science **40**, 1051–1060 (1985).

[27] V. Carey, "Dependence of settling velocity on particle concentration in a fluidized bed of spherical particles," International Journal of Multiphase Flow **13**, 429–431 (1987).

[28] J. Richardson and W. Zaki, "Sedimentation and fluidisation: Part i," Chemical Engineering Research and Design **75**, S82–S100 (1997).

[29] P. Meliga, J. M. Chomaz, and D. Sipp, "Unsteadiness in the wake of disks and spheres: Instability, receptivity and control using direct and adjoint global stability analyses," Journal of Fluids and Structures **25**, 601–616 (2009).

[30] B. Pier, "Local and global instabilities in the wake of a sphere," Journal of Fluid Mechanics **603**, 39–61 (2008).

[31] D. Fabre, F. Auguste, and J. Magnaudet, "Bifurcations and symmetry breaking in the wake of axisymmetric bodies," Physics of Fluids **20** (2008), 10.1063/1.2909609.

[32] V. Citro, L. Siconolfi, D. Fabre, F. Giannetti, and P. Luchini, "Stability and sensitivity analysis of the secondary instability in the sphere wake," AIAA Journal **55**, 3661–3668 (2017).

[33] K. Gumowski, J. Miedzik, S. Goujon-Durand, P. Jenffer, and J. Wesfreid, "Transition to a time-dependent state of fluid flow in the wake of a sphere," Physical Review E **77**, 055308 (2008).

[34] I. P. Castro, “Wake characteristics of two-dimensional perforated plates normal to an air-stream,” Journal of Fluid Mechanics **46**, 599–609 (1971).

[35] L. Zong and H. Nepf, “Vortex development behind a finite porous obstruction in a channel,” Journal of Fluid Mechanics **691**, 368–391 (2012).

[36] A. Nicolle and I. Eames, “Numerical study of flow through and around a circular array of cylinders,” Journal of Fluid Mechanics **679**, 1–31 (2011).

[37] K. Steiros and M. Hultmark, “Drag on flat plates of arbitrary porosity,” Journal of Fluid Mechanics **853**, R3 (2018).

[38] K. Steiros, N. Bempedelis, and L. Ding, “Recirculation regions in wakes with base bleed,” Physical Review Fluids **6**, 034608 (2021).

[39] K. Steiros, K. Kokmanian, N. Bempedelis, and M. Hultmark, “The effect of porosity on the drag of cylinders,” J. Fluid Mech **901**, R2 (2020).

[40] G. Zampogna and F. Gallaire, “Effective stress jump across membranes,” Journal of Fluid Mechanics **892**, A9 (2020).

[41] R. Hajian and J. W. Jaworski, “The steady aerodynamics of aerofoils with porosity gradients,” Proceedings of the Royal Society A: Mathematical, Physical and Engineering Sciences **473**, 20170266 (2017).

[42] P. J. Baddoo, R. Hajian, and J. W. Jaworski, “Unsteady aerodynamics of porous aerofoils,” Journal of Fluid Mechanics **913** (2021).

[43] C. Cummins, I. Viola, E. Mastropaolo, and N. Nakayama, “The effect of permeability on the flow past permeable disks at low Reynolds numbers,” Physics of Fluids **29** (2017), 10.1063/1.5001342.

[44] E. F. Strong, M. Pezzulla, F. Gallaire, P. Reis, and L. Siconolfi, “Hydrodynamic loading of perforated disks in creeping flows,” Phys. Rev. Fluids **4**, 084101 (2019).

[45] T. Tang, J. Xie, S. Yu, J. Li, and P. Yu, “Effect of aspect ratio on flow through and around a porous disk,” Phys. Rev. Fluids **6**, 074101 (2021).

[46] P. G. Ledda, L. Siconolfi, F. Viola, F. Gallaire, and S. Camarri, “Suppression of von Kármán vortex streets past porous rectangular cylinders,” Phys. Rev. Fluids **3**, 103901 (2018).

[47] T. Tang, P. Yu, X. Shan, and H. Chen, “The formation mechanism of recirculating wake for steady flow through and around arrays of cylinders,” Physics of Fluids **31**, 043607 (2019).

[48] T. Tang, P. Yu, X. Shan, J. Li, and S. Yu, “On the transition behavior of laminar flow through and around a multi-cylinder array,” Physics of Fluids **32**, 013601 (2020).

[49] P. Yu, Y. Zeng, T. S. Lee, X. B. Chen, and H. T. Low, “Numerical simulation on steady flow around and through a porous sphere,” International Journal of Heat and Fluid Flow **36**, 142–152 (2012).

[50] M. Pezzulla, E. F. Strong, F. Gallaire, and P. M. Reis, “Deformation of porous flexible strip in low and moderate Reynolds number flows,” Phys. Rev. Fluids **5**, 084103 (2020).

[51] Y. Sato and Y. Hattori, “Mechanism of reduction of aeroacoustic sound by porous material: comparative study of microscopic and macroscopic models,” Journal of Fluid Mechanics **929** (2021).

[52] C. Teruna, F. Avallone, D. Ragni, and D. Casalino, “On the noise reduction of a porous trailing edge applied to an airfoil at lifting condition,” Physics of Fluids **33**, 055132 (2021).

[53] C. Teruna, F. Avallone, D. Ragni, A. Rubio-Carpio, and D. Casalino, “Numerical analysis of a 3-d printed porous trailing edge for broadband noise reduction,” Journal of Fluid Mechanics **926** (2021).

[54] D. Josef and L. Tao, “The effect of permeability on the slow motion of a porous sphere in a viscous liquid,” Zamm **44**, 361–364 (1964).

[55] G. Neale, N. Epstein, and W. Nader, “Creeping flow relative to permeable spheres,” Chemical Engineering Science **28**, 1865–1874 (1973).

[56] P. Adler, “Streamlines in and around porous particles,” Journal of Colloid and Interface Science **81**, 531–535 (1981).

[57] H. Darcy, *Les fontaines publiques de la ville de Dijon: exposition et application des principes a suivre et des formules a employer dans les questions de distribution d’eau* (Victor Dalmont, Paris, 1856).

[58] H. C. Brinkman, “A calculation of the viscous force exerted by a flowing fluid on a dense swarm of particles,” Flow, Turbulence and Combustion **1**, 27 (1949).

[59] X. Chu, Y. Wu, U. Rist, and B. Weigand, “Instability and transition in an elementary porous medium,” Physical Review Fluids **5**, 044304 (2020).

[60] S. Whitaker, *The Method of Volume Averaging* (Jacob Bear, Technion – Israel Institute of Technology., 1998).

[61] S. Whitaker, “The forchheimer equation: A theoretical development,” Transport in Porous Media **25**, 27–61 (1996).

[62] G. A. Zampogna and A. Bottaro, “Fluid flow over and through a regular bundle of rigid fibres,” Journal of Fluid Mechanics **792**, 5–35 (2016).

[63] U. Lācis and S. Bagheri, “A framework for computing effective boundary conditions at the interface between free fluid and a porous medium,” J. Fluid Mech. **812**, 866–889 (2017).

[64] U. Lācis, G. Zampogna, and S. Bagheri, “A computational continuum model of poroelastic beds,” Proceedings of the Royal Society A: Mathematical, Physical and Engineering Sciences **473**, 20160932 (2017).

[65] U. Lācis, Y. Sudhakar, S. Pasche, and S. Bagheri, “Transfer of mass and momentum at rough and porous surfaces,” Journal of Fluid Mechanics **884**, A21 (2020).

[66] P. G. Ledda, E. Boujo, S. Camarri, F. Gallaire, and G. Zampogna, “Homogenization-based design of microstructured membranes: wake flows past permeable shells,” Journal of Fluid Mechanics **927**, A31 (2021).

[67] A. Bottaro, “Flow over natural or engineered surfaces: an adjoint homogenization perspective,” Journal of Fluid Mechanics **877**, P1 (2019).

[68] S. B. Naqvi and A. Bottaro, “Interfacial conditions between a free-fluid region and a porous medium,” International Journal of Multiphase Flow **141**, 103585 (2021).

[69] G. A. Zampogna, J. Magnaudet, and A. Bottaro, “Generalized slip condition over rough surfaces,” Journal of Fluid Mechanics **858**, 407–436 (2019).

[70] G. K. Batchelor and A. E. Gill, “Analysis of the stability of axisymmetric jets,” Journal of Fluid Mechanics **14**, 529–551 (1962).

[71] F. Viola, G. Iungo, S. Camarri, F. Porté-Agel, and F. Gallaire, “Prediction of the hub vortex instability in a wind turbine wake: stability analysis with eddy-viscosity models calibrated on wind tunnel data,” Journal of Fluid Mechanics **750**, R1 (2014).

[72] A. Quarteroni, “Domain decomposition methods,” in *Numerical Models for Differential Problems* (Springer International Publishing, Cham, 2017) pp. 555–612.

[73] P. Yu, Y. Zeng, T. S. Lee, X. B. Chen, and H. T. Low, “Steady flow around and through a permeable circular cylinder,” Computers & Fluids **42**, 1–12 (2011).

[74] P. Monkewitz, “The absolute and convective nature of instability in two dimensional wakes at low Reynolds numbers,” The Physics of Fluids **31**, 999–1006 (1988).

[75] P. Luchini and A. Bottaro, “Adjoint equations in stability analysis,” Annual Review of Fluid Mechanics **46**, 493–517 (2014).

[76] J. Schulze and J. Sesterhenn, “Optimal distribution of porous media to reduce trailing edge noise,” Computers & Fluids **78**, 41–53 (2013), lES of turbulence aeroacoustics and combustion.

[77] D. Harrison, “Fluidization,” Science Progress (1933-) **61**, 191–217 (1974).